Large-eddy simulation of three-dimensional dunes in a steady, unidirectional flow. Part 1: Turbulence statistics.

Mohammad Omidyeganeh and Ugo Piomelli

Department of Mechanical and Materials Engineering, Queen's University, Kingston (Ontario) K7L 3N6, Canada

(Received 9 March 2015)

We performed large-eddy simulations of flow over a series of three-dimensional dunes at laboratory scale (Reynolds number based on the average channel depth and streamwise velocity was 18,900) using the Lagrangian dynamic eddy-viscosity subgrid-scale model. The bedform three-dimensionality was imposed by shifting a standard two-dimensional dune shape in the streamwise direction according to a sine wave. The statistics of the flow are discussed in ten cases with in-phase and staggered crestlines, different deformation amplitudes and wavelengths. The results are validated qualitatively against experiments. The three-dimensional separation of flow at the crestline alters the distribution of wall pressure, which in turn may cause secondary flow across the stream, which directs low-momentum fluid, near the bed, toward the lobe (the most downstream point on the crestline) and high-momentum fluid, near the top surface, toward the saddle (the most upstream point on the crestline). The mean flow is characterized by a pair of counter-rotating streamwise vortices, with core radius of the order of the flow depth. However, for wavelengths smaller than the flow depth, the secondary flow exists only near the bed and the mean flow away from the bed resembles the two-dimensional case. Staggering the crestlines alters the secondary motion; the fastest flow occurs between the lobe and the saddle planes, and two pairs of streamwise vortices appear (a strong one, centred about the lobe, and a weaker one, coming from the previous dune, centred around the saddle). The distribution of the wall stress and the focal points of separation and attachment on the bed are discussed. The sensitivity of the average reattachment length, depends on the induced secondary flow, the streamwise and spanwise components of the channel resistance (the skin friction and the form drag), and the contribution of the form drag to the total resistance are also studied. Three-dimensionality of the bed increases the drag in the channel; the form drag contributes more than in the two-dimensional case to the resistance, except for the staggered-crest case. Turbulent-kinetic energy is increased in the separated-shear layer by the introduction of three-dimensionality, but its value normalized by the plane-averaged wall stress is lower than in the corresponding two-dimensional dunes. The upward flow on the stoss side and higher deceleration of flow on the lee side over the lobe plane lift and broaden the separated-shear layer, respectively, affecting the turbulent kinetic energy.

1. Introduction

The interaction of a turbulent flow with a mobile sand bed results in a deformation of the bed, whose shape depends on the amount of sand available and on the flow properties.

At stable flow conditions in rivers with mobile sand bed, equilibrium bed shapes are eventually reached from an arbitrary bedform; at sub-critical flow-rates, they are called either ripples or dunes (van Rijn 1984). Ripples are small-scale (compared to the flow depth) deformations, and can be treated as increased roughness that does not affect turbulence far from the bed. Dunes, on the other hand, are large-scale deformations that affect turbulence throughout the depth. At higher flow velocities (hence larger Froude numbers) ripples are transitioned to dunes, where the dominant sediment transport mechanism is bed-load transport (Yalin 1964). Dunes have asymmetric shapes in the streamwise direction with a sharp downward slope called "lee side" and a gentle upward slope called "stoss side" (Kostaschuk 2000).

We concentrate here on dune dynamics, although many of the features also apply to ripples. Dunes can take two-dimensional (2D) or three-dimensional (3D) shapes. In rivers, at low flow-discharge rates, 2D dunes are formed with regular wavelength and height. The time required for dunes to be generated at steady flow conditions is at most a few hours (Venditti *et al.* 2005). At high velocities and Reynolds numbers, on the other hand, dunes have highly sinusoidal or irregular crestlines (Ashley 1990). The Reynolds number is not the only factor to determine the shape of the bed. Modifications in flow structures, such as geometry changes by an object or turbulence-induced secondary flows, can trigger modifications in the bedforms that eventually result in 3D dunes (Allen 1968). The total amount of transported sediment, which is a function of the bed shear stress and time, plays a major role in evolution of 3D bedforms (Baas *et al.* 1993; Baas 1994, 1999).

The transition from one bedform to another may be caused by an increase of a few cm/s in the flow velocity (Venditti *et al.* 2005), but usually occurs gradually, like the transition of ripples to dunes (Bennett & Best 1996; Robert & Uhlman 2001; Schindler & Robert 2005). In general, the transition of a bedform depends both on the flow-rate and the time required for the bed defects to grow. The reason 3D bedforms exist at high flow discharge may simply be that it takes less time to move the sediment required for the transition (Venditti *et al.* 2005). Even bedforms developed in wide flumes may become 3D over time; therefore, the idea that persistent 2D features develop at lower flow strengths is not completely true (Venditti *et al.* 2005), and may be due to the run-times used in some experiments, which may be too short to allow the transition to 3D bed forms, as shown by the transition of 2D to 3D ripples over time (Baas *et al.* 1993; Baas 1994, 1999). Another possible reason why stable 2D bedforms have been reported is the use of narrow flumes, since the mean eddy size is of the order of the flume width, and 3D morphology could not easily be established (Venditti *et al.* 2005). Sometimes the three-dimensionality of dunes is negligible compared to the height of the bed, hence they are considered as 2D, especially in field studies (Babakaiff & Hickin 1996).

Although flow over dunes has been extensively studied in field experiments (Matthes 1947; Jackson 1976; Flemming 1978; Gabel 1993; Kostaschuk & Church 1993; Bennett & Best 1995; Babakaiff & Hickin 1996; Kostaschuk & Villard 1996; Roden 1998; Carling *et al.* 2000; Kostaschuk 2000; Best *et al.* 2001), fixed 2D dunes have been the focus of the studies in laboratory experiments (Müller & Gyr 1986; Nelson *et al.* 1993; Kadota & Nezu 1999; Schmeeckle *et al.* 1999; Venditti & Bennett 2000; Hyun *et al.* 2003; Balachandar *et al.* 2007; Balachandar & Patel 2008), numerical simulations (Yoon & Patel 1996; Schmeeckle *et al.* 1999; Yue *et al.* 2005; Polatel *et al.* 2006; Yue *et al.* 2006; Stoesser *et al.* 2008; Grigoriadis *et al.* 2009; Omidyeganeh & Piomelli 2011), as well as theoretical studies (McLean & Smith 1986; Nelson & Smith 1989; McLean *et al.* 1999). A comprehensive review of literature on dunes is given by Best (2005). The flow separates at the dune crest, generates a shear layer that plays a crucial role in the transport of momentum and energy, and the generation of coherent structures (Omidyeganeh & Piomelli 2011). An internal

boundary layer is developed after reattachment on the stoss side, and a wake region behind the recirculation zone extends toward the downstream dune. The flow decelerates over the lee side and then accelerates over the stoss side. These characteristics of the mean flow and statistics were common in almost all turbulent flow studies of 2D dunes (Venditti & Bauer 2005).

Although 3D dunes exist almost everywhere in rivers, the effects of their geometry on flow dynamics are still unknown. As stated by Best (2005), the relation between boundary shear stress, turbulence statistics, and three-dimensionality of dunes must be studied to explore the morphology mechanics and channel resistance in rivers, to help us understand the transition from 2D to 3D dunes. In this work, we perform a numerical study of this problem, to investigate the sensitivity of fluid mechanical parameters to 3D parameters of bed forms.

The early work of Allen (1968), who presented a variety of three-dimensional bedforms and their near-bed streamlines, revealed insights into the bed deformation properties observed in nature. The quantitative study of the turbulent flows over 3D bedforms, however, did not begin until the past decade, when Zedler & Street (2001) conducted a numerical study of the flow over small-scale wavy 3D bed deformations. They were able to resolve near-bed Görtler vortices, which accumulate sediment in areas with upward mean-flow motion.

Maddux *et al.* (2003*a*,*b*) examined the flow over straight-troughed dunes with 180^o out-of-phase sinusoidal cross-stream variation in dune height. By maintaining a constant lee slope, the fixed dune crests curved across the channel forming saddles at elevated crest points, and lobes at shortened crest points. The length of dunes was $20h$, where h is the average dune height. A cosine wave was imposed on the crest height, with wavelength equal to the flume width, $\lambda = 22.5h$ and amplitude half of the average dune height, $A = h/2$. Their measurements were conducted for two cases with deep ($H = 14.0h$) and shallow ($H = 4.3h$) flow with Reynolds numbers $Re = 112,000$ and $47,000$ based on average bulk velocity and average flow depth. The flow resistance was higher by almost 50% over the 3D dunes, but the turbulence intensity was much lower. Maddux *et al.* (2003*a*,*b*) also examined the free-surface response to bed-shape configuration and observed, for the 3D dunes, 2D free-surface deformations similar to those observed over 2D dunes. The maximum deviation of the free-surface level from the averaged straight level was 2.5% of the average dune height. The phase difference in the crestlines results into a sequence of saddles between the lobes. The flow moved away from this high-low crest sequence region, which acted as a virtual vertical plane normal to the spanwise direction and at the middle of the flume. Hence, the greatest streamwise velocity occurred over the nodes, between the saddle and the lobe. The cross-stream flow was stronger close to the bed and over the nodes, while the upward velocity was higher upstream of the saddle where the highest crest exists. The decelerated flow over the saddle resulted in a larger separation cell than in a typical 2D dune case at the same Reynolds number; the cross-stream flow near the bed was found to be in an opposite direction to the flow near the free surface. Maddux *et al.* (2003*a*,*b*) conjectured that the secondary flow across the stream is caused by turbulence asymmetry. The integral of the momentum balance equation was examined to partition the total drag into its subcomponents, form and viscous drag. Despite a good estimation of form drag and bottom pressure, the skin-friction estimation from the near-bed mean velocity and Reynolds shear stress was not accurate. The largest form drag and skin friction were observed over the node, where the streamwise velocity is largest. Relatively higher boundary shear-stress accompanied by lower Reynolds shear stress indicate the importance of precise measurements and calculations of shear stresses for sediment transport prediction. The field observations

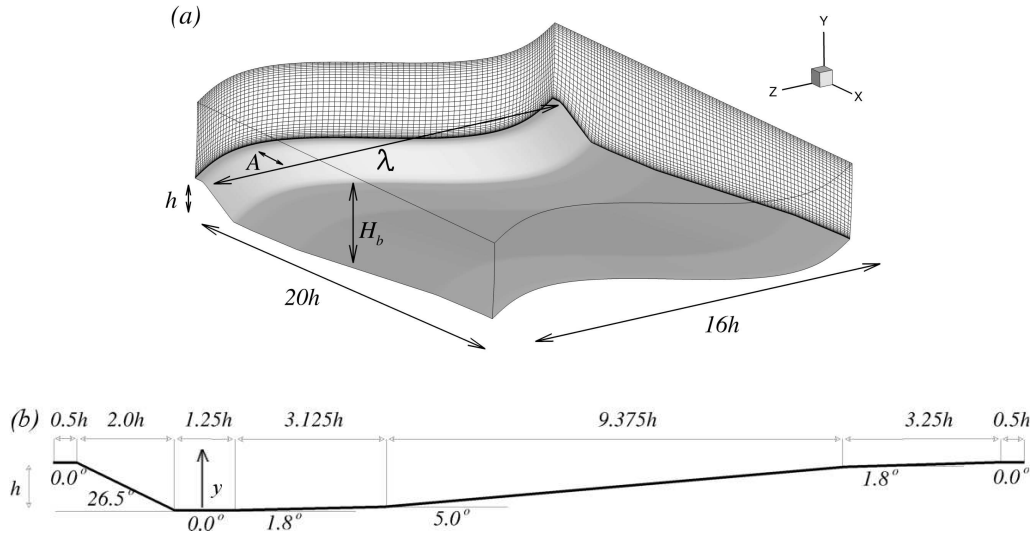

FIGURE 1. *(a)* Sketch of the physical 3D dune configuration. The sine function that is superimposed into 2D dune configuration is $A\sin(2\pi z/\lambda)$, where λ is the wavelength (here $\lambda = 16h$) and A is the amplitude (here $A = 2h$), and *(b)* bed geometry.

of Parsons *et al.* (2005) highlight the importance of 3D bedforms for flow structures and sediment transport. Secondary flows over saddle- or lobe- shaped crestlines were observed to be larger and more structured, and direct the downstream bed morphology and sediment-suspension mechanism in the flow. Parsons *et al.* (2005) suggest that in the case of smaller scale macro-turbulence in flows over 3D dunes, suspension of bed sediment may be less, affecting the bed morphology significantly. There is a need to quantify the scales of vortical structures in flows over various 3D dunes to evaluate this conjecture.

The effect of different 3D bedforms has been investigated by Venditti (2007) using fixed 2D and 3D dune morphologies. The main difference between the 3D dunes used in his work and those used by Maddux *et al.* (2003*a*,*b*) is the way the three-dimensionality was introduced, by deforming the crestline in the streamwise (rather than in the vertical) direction, similar to the geometry used in the present simulations, illustrated in Figure 1; this placed saddles at the most upstream spanwise locations of the crestline, and lobes at the most downstream position. In the experiments of Venditti (2007), the downstream crestline was in phase with the upstream one. The dune length was $20h$ and the average flow depth was close to $6.8h$; the Reynolds number of the experiment was $Re = 73,010$ based on the average flow depth and the average bulk velocity. In the case of full-width saddle or full-width lobe dunes, a constant oblique line with the slope of almost 1.1 was used, while for the case of sinusoidal crestline, a sine wave with $A = 2.33h$ and $\lambda = 11.45h$ was introduced. The sinuosity of the crestline is defined in terms of a non-dimensional span number, NDS= L_c/L_y (Venditti *et al.* 2005), where L_c is the crestline length and L_y is the linear distance between the crest endpoints (in the experiment, this was equal to the channel width). Observations were not consistent with those of Maddux *et al.* (2003*b*), since the crestlines were in phase. The flow was fastest over the saddle and slowest over the lobe, while turbulence was highest over the lobe and lowest over the saddle. By looking at the spatially-averaged vertical and spanwise velocities, a secondary flow pattern was conjectured in which flow moves upward over the lobe and downward over the saddle. From these mean-flow and turbulence distributions, the author concluded

that a stable configuration of 3D dunes with sinusoidal crestlines can be formed with 180^o phase difference in sinuous profiles, like those of Maddux *et al.* (2003*a*,*b*).

The importance of 3D dunes in controlling the flow resistance, sediment transport, and turbulence production demands a closer study of the flow mechanics. Experiments conducted so far on 3D dunes lack precise measurements of near-wall quantities, including skin friction and form drag, as well as spatially-resolved turbulent stresses. We performed, therefore, a controlled investigation that begins from typical 2D dunes and develops more complicated bedforms. Starting from a simple sinusoidal crestline deformation, we incorporate common dune configurations, maintaining similarity to our previous study on 2D dunes (Omidyeganeh & Piomelli 2011) as well as to recent measurements of flows over 3D dunes (Maddux *et al.* 2003*a*,*b*; Venditti 2007). In addition to the total boundary shear stress, its subcomponents must be determined for prediction of various natural phenomena such as sediment transport rates that affects the stability of dunes (since the skin friction directly contributes to the sediment transport, while form drag does not). This work is the first effort in simulating turbulent flows over 3D dunes and reveals new understanding of flow mechanics that could not be measured in experiments. The variety of cases studied enables comprehensive investigation on the effects of three-dimensionality on flow resistance and turbulence statistics. While this paper is focussed on turbulence statistics for the flows over various 3D dunes, a follow-up article will present details of the coherent vortical structures and analyze their characteristics qualitatively and quantitatively.

2. Problem formulation

In large-eddy simulations, the velocity field is separated into a resolved (large-scale) and a subgrid (small-scale) field, by a spatial filtering operation (Leonard 1974). The non-dimensionalized continuity and Navier-Stokes equations for the resolved velocity field are

$$\frac{\partial \overline{u}_i}{\partial x_i} = 0 \tag{2.1}$$

$$\frac{\partial \overline{u}_i}{\partial t} + \frac{\partial \overline{u}_i \overline{u}_j}{\partial x_j} = -\frac{\partial \overline{P}}{\partial x_i} - \frac{\partial \tau_{ij}}{\partial x_j} + \frac{1}{Re_b}\frac{\partial^2 \overline{u}_i}{\partial x_j \partial x_j} \tag{2.2}$$

where $Re_b = U_b H_b/\nu$, H_b is the average channel depth, and U_b is the bulk velocity at the streamwise location where the channel depth is equal to the average channel depth ($x \approx 14h$). x_1, x_2 and x_3 are the streamwise, vertical and spanwise directions, also referred to as x, y and z. The velocity components in these directions are, respectively, u_1, u_2 and u_3 (or u, v and w). An overline denotes a filtered quantity, and $\tau_{ij} = \overline{u_i u_j} - \overline{u}_i \overline{u}_j$ are the subgrid stresses, which were modeled using an eddy-viscosity assumption

$$\tau_{ij} - \delta_{ij}\tau_{kk}/3 = -2\nu_T \overline{S}_{ij} = -2C\overline{\Delta}2|\overline{S}|\overline{S}_{ij}. \tag{2.3}$$

Here, $\overline{\Delta} = 2\left(\Delta x \Delta y \Delta z\right)^{1/3}$ is the filter size, $\overline{S}_{ij} = \left(\partial \overline{u}_i/\partial x_j + \partial \overline{u}_j/\partial x_i\right)/2$ is the resolved strain-rate tensor and $|\overline{S}| = \left(2\overline{S}_{ij}\overline{S}_{ij}\right)^{1/2}$ is its magnitude. The coefficient C is determined using the dynamic model (Germano *et al.* 1991) with the Lagrangian averaging technique proposed by Meneveau *et al.* (1996), and extended to non-Cartesian geometries by Jordan (1999) and Armenio & Piomelli (2000).

The governing differential equations (2.1) and (2.2) are discretized on a non-staggered grid using a curvilinear finite-volume code. The method of Rhie & Chow (1983) is used to avoid pressure oscillations. Both convective and diffusive fluxes are approximated by second-order central differences. A second-order-accurate semi-implicit fractional-step

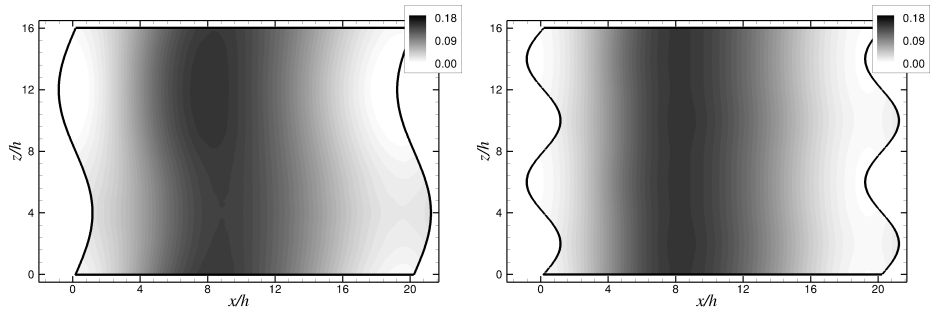

FIGURE 2. Contours of mean pressure, $\overline{P}/U_b^2$, on the top surface of Case 2 (left) and case 5 (right) defined in Table 1.

procedure (Kim & Moin 1985) is used for the temporal discretization. The Crank-Nicolson scheme is used for the wall-normal diffusive terms, and the Adams-Bashforth scheme for all the other terms. The pressure is obtained from the solution of a Poisson equation, which will be discussed later. The code is parallelized using the Message-Passing Interface and the domain-decomposition technique, and has been extensively tested for turbulent flows (Silva Lopes & Palma 2002; Silva Lopes *et al.* 2006; Radhakrishnan *et al.* 2006, 2008; Omidyeganeh & Piomelli 2011).

Dunes are known to have a wavelength equal to 5-6 times the flow depth, and height equal to 1/4 of the flow depth. For this reason, most dune shapes studied experimentally and numerically are quite similar. We base our geometry on the 2D one used by Balachandar *et al.* (2007). A sinusoidal wave in the spanwise direction with an amplitude A, and a wavelength λ is superimposed on the streamwise position of all points in the domain. The computational configuration is sketched in Figure 1. Periodic boundary conditions are used in the streamwise (x) and spanwise (z) directions. The flow is driven by a pressure gradient that maintains a constant streamwise flow-rate in time. The top surface is assumed to be rigid and free of shear stress: the vertical velocity is set to zero, as are the vertical derivatives of the streamwise and spanwise velocity components. The surface deformation is reported to be small, less than 2% of the flow depth in experiments (McLean *et al.* 1994; Kadota & Nezu 1999; Maddux *et al.* 2003*b*,*a*) and simulations (Yue *et al.* 2006; Stoesser *et al.* 2008) of 2D and 3D dunes, and it was shown (Maddux *et al.* 2003*b*) that the free surface response to the 3D dune bed is 2D. The pressure distribution on the top surface calculated in the current simulations (Figure 2) presents negligible dependency on the spanwise deformation of the bed. Therefore, the free-slip condition is expected to have small effects on the statistics and on the evolution of significant structures. The Reynolds number is $18,900$ based on the $H_b \simeq 3.5h$ and U_b defined above.

An orthogonal mesh in the $xy-$plane is generated using a hyperbolic grid-generation technique. This mesh is then repeated in the spanwise direction with non-uniform spacing as discussed below, superimposed with a sine function shift, $A\sin(2\pi z/\lambda)$, in the streamwise direction.

In our previous simulations of 2D dunes, the grid lines parallel to the z axis were straight, and the spacing was uniform. This implied that, in the Poisson equation for pressure, the only term involving z was of the form $\partial^2/\partial z^2$; this allowed us to take a Fourier Transform of the Poisson equation in the z direction, which decoupled the system, and allowed us to solve $N_z/2$ (complex) bi-dimensional systems of size $N_x \times N_y$ by a BiConjugate Gradient Stabilized (BiCGStab) method, instead of the coupled $N_x \times$

$N_y \times N_z$ system. To preserve the advantages of the decoupling in this work, in which the grid lines in the z direction are not straight, but follow the sinusoidal crestline, we had to modify the method described above.

The non-orthogonality of the grid lines to the $xy-$planes introduces, in the Poisson equation in the transformed space (ξ, η, ζ), cross-derivative terms of the form $\partial^2/\partial\xi\partial\zeta$, where ξ, η, and ζ are grid-line tangent coordinates in the direction of increment of indices i, j, and k, respectively. Applying the Fourier Transform to these terms would not result in a decoupled system. We, therefore, adopt an iterative approach. First, we consider a grid that is equispaced in ζ:

$$\Delta\zeta(i,j,k) = |\mathbf{x}(i,j,k+1) - \mathbf{x}(i,j,k)| = \text{constant}. \tag{2.4}$$

This condition requires non-uniform grid spacing in the spanwise direction, with coarser mesh around the saddle and the lobe planes, and finer mesh in between. Second, we consider the cross terms as known (we calculate them using the pressure at the previous time-step initially) and move them to the right-hand-side of the Poisson equation; then we apply the Fourier transform, and solve the decoupled system using BiCGStab. The resulting pressure is then used to re-compute the cross terms, and the system is solved again until convergence. Three iterations were generally sufficient. This technique was validated by simulating a 2D turbulent channel flow, using a grid skewed in the spanwise direction (more skewed than any of those used in the present study) and was found to be accurate and efficient.

Based on the bed-shape characteristics, Venditti *et al.* (2005) found the transition of 2D dunes into 3D dunes to occur when NDS$\simeq$ 1.2. We want to observe the transition in the flow characteristics as the amplitude and the wavelength of the sine wave is changed; therefore, keeping channel dimensions, Reynolds number and the geometry, unchanged, the effects of the amplitude A and the wavelength λ on flow characteristics are studied. Table 1 lists all test cases; A and λ are changed slowly to observe transition from 2D to 3D dunes clearly; the NDS values are also reported, and bracket the critical value. Case 10 is the only simulation with two dunes in series to study 3D dunes with crestlines having 180^o phase difference. This is close to the experiment by Maddux *et al.* (2003*a*,*b*) and to natural bedforms.

The number of grid points in Cases 1 to 9 is $256 \times 96 \times 256$; this number is higher than used in our previous simulation of 2D dunes (Omidyeganeh & Piomelli 2011), to compensate for the non-uniformity in grid spacing caused by sinuosity of the crestline. The average grid spacings for each case are also included in Table 1, illustrating acceptable resolution for a typical LES. Validation of the numerical model was difficult, since no experiment is available in flow conditions similar to those used here. However, some confidence in the data can be achieved by observing that the current problem is similar to the 2D simulation (Omidyeganeh & Piomelli 2011), which has been validated extensively against experiment and simulation (Stoesser *et al.* 2008). In that paper, we examined average velocities and Reynolds stresses along six vertical lines in the channel with those in previous simulation and experiment, and excellent agreement was obtained. Contours of turbulence statistics on the xy-planes also showed remarkable agreement with previous work (Stoesser *et al.* 2008; Grigoriadis *et al.* 2009). Furthermore, a grid refinement study was performed for Cases 2 and 5, in which $384 \times 128 \times 384$ grid points were used; first- and second-order statistics were within 5% of each other. A comparison of the velocity profiles will be shown later.

The equations were integrated for $500h/U_b$ time units to remove transient effects. Then, statistics were accumulated over $2000h/U_b$ time units. To increase the sample size, averaging was also performed over the symmetric points in the spanwise direction. To

Case No.	λ/h	A/h	NDS	Δs^+_{avg}	Δn^+_{avg}	Δz^+_{avg}
1	16.0	0.5	1.01	21.3	0.7	17.1
2	16.0	1.0	1.04	22.1	0.7	18.2
3	16.0	2.0	1.14	23.6	0.8	21.4
4	8.0	0.5	1.04	21.6	0.7	17.8
5	8.0	1.0	1.14	22.5	0.7	20.3
6	8.0	1.5	1.29	23.3	0.8	23.8
7	8.0	1.7	1.36	23.8	0.8	25.6
8	8.0	2.0	1.46	24.2	0.8	28.1
9	4.0	1.0	1.46	22.4	0.7	25.9
10	16.0	1.0	1.04	17.6	0.7	14.0

TABLE 1. Properties of the test cases. For the definition of the variables λ and A refer to the caption of Figure 1. Case 10 has two dunes in series in the streamwise direction with 180^o phase shift in the cosine function of the crestline.

verify the adequacy of the sample, we compared statistics obtained using only half of the sample with those obtained using the complete sample, and found that the mean velocities differed by less than 1%, and the root-mean-square (rms) intensities by less than 5%.

3. Results

3.1. *Mean-flow characteristics*

Figure 3 illustrates the mean-flow streamlines tangential to three vertical planes at the lobe (L), node (N), and saddle (S) of the 3D geometry (*i.e.*, obtained using only the velocity components in the plane). We concentrate herein on Case 5, and qualitative differences with the other cases will be shown whenever they are significant. Contours of streamwise velocity in Figure 3 show that the fluid separates over the crest, forming a recirculation bubble on the lee side of the dune. At the saddle and node, the flow then reattaches on the stoss side, similar to what is observed in the 2D case (Kostaschuk & Church 1993; Nelson *et al.* 1993; Nezu & Nakagawa 1993; McLean *et al.* 1994; Bennett & Best 1995; Schmeeckle *et al.* 1999; Venditti & Bauer 2005; Stoesser *et al.* 2008; Grigoriadis *et al.* 2009; Omidyeganeh & Piomelli 2011), but the behaviour at the lobe is different. The separation streamline never reaches the wall: fluid coming from the saddle region near the wall displaces it upwards, and a saddle point (point C in Figure 3*(a)*) is formed at the beginning of the stoss side on the lobe plane. This phenomenon is caused by the

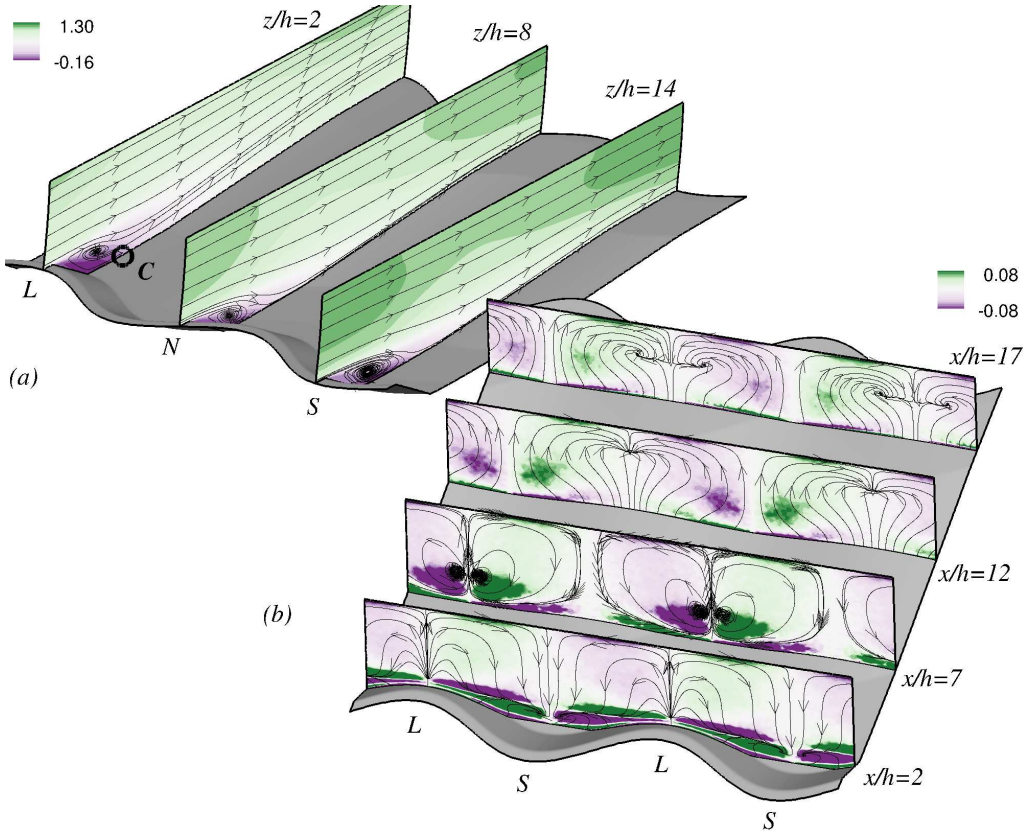

FIGURE 3. Case 5. *(a)* Mean-flow streamlines and mean streamwise-velocity contours, U/U_b, on three $xy-$planes. *(b)* Secondary-flow streamlines and mean streamwise vorticity contours, $\Omega_x h/U_b$, on four $yz-$planes.

spanwise pressure gradient generated by the three-dimensionality, and depends critically (as will be shown later) on the details of the dune crest shape. Also note that the flow over the lobe is slower than that over the saddle and node regions. The difference in the momentum available to the fluid may also play a role in the separation/reattachment behaviour. Note that in the following we will refer to "reattachment point" as the point where the streamwise component of the wall stress becomes positive, even if the separated streamline does not reattach, as is the case in some 3D separated flows.

Figure 4 shows the streamlines tangent to a plane near the bed, which are consistent with the observations of Allen (1968), who used plaster for flow visualization (see Figure 12.8 in Allen (1968)). On the lee side of the dune, the spanwise pressure gradient is directed from the lobe to the saddle, while further downstream it is positive from the saddle to the lobe, resulting in the near-wall motion described above. Over the stoss side, before and after the reattachment, the spanwise pressure gradient is directed from the saddle towards the lobe. This secondary flow near the bed results in the saddle point of separation over the lobe plane (point C in Figure 3(a), and points S_s in Figure 4) and inhibits the reattachment of the separated flow over the lobe. Symmetric 3D separation lines result in "Type I" separation with symmetry breaking discussed by Chapman & Yates (1991), in which a saddle point of separation (S_s^1 in Figure 4) at the upstream point on the line and a nodal point of separation (N_s in Figure 4) at the downstream

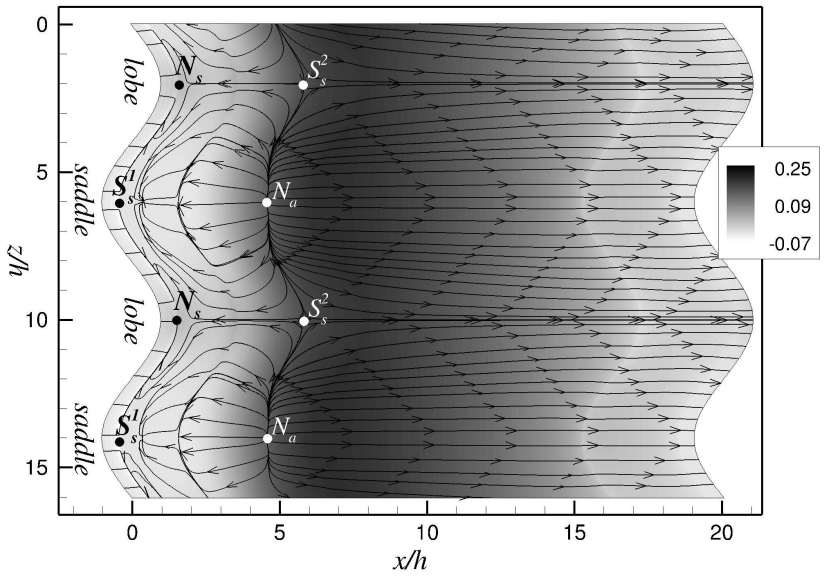

FIGURE 4. Mean-flow streamlines and mean pressure contours, $\overline{P}/U_b^2$, on a plane at constant distance from the bed, with $y^+ \approx 3$ on the average for Case 5. The primary nodes and separations are illustrated by N_s, nodal separation; S_s, saddle separation; N_a, nodal attachment (Chapman & Yates 1991)

point appear. This type of separation induces a nodal point of attachment (N_a in Figure 4) downstream of S_s^1 in the symmetry plane (the saddle plane) and a saddle point of separation (S_s^2 in Figure 4) downstream of N_s in the symmetry plane (the lobe plane). We will show that the S_s^2 points over the lobe plane cause the deformation of the reattachment line (based on our definition), known as "bulging". Note that discontinuities on the lee side of the dune are caused by the sudden change of bed slope.

The spanwise pressure-gradient caused by 3D separation also results in the secondary flow shown in Figure 3*(b)*. Low-momentum fluid near the bed moves away from the saddle plane towards the lobe, while high-momentum fluid moves away from the lobe towards the saddle. The streamwise average of the cross-stream flow over a dune length (Figure 12*(b)* in Venditti (2007)) is qualitatively the same as the current results. The secondary flow is fairly weak (the in-plane velocity is less than 12% of the streamwise velocity) but affects significantly form drag and skin friction. Sediment transport is also affected by this motion, similar to secondary flows over 3D ripples (Zedler & Street 2001) in which sediment is suspended in the areas with near-bed upward motions (in the lobe plane in the current simulations). As high-speed fluid converges over the saddle from the free surface and moves down toward the bed for almost half the dune height at $x/h = 12$, the maximum value of the streamwise velocity occurs below the surface. This phenomenon, known as "velocity dip", is observed in most secondary flows (Nezu & Nakagawa 1993) in open channels, in experiments (Venditti 2007), and in the present study for Cases 1 through 8. Cases 9 (very short wavelength) and 10 (staggered lobes and saddles) have different physics that will be discussed later.

Mean-velocity profiles over the saddle and the lobe planes are compared to the profiles over 2D dunes (Omidyeganeh & Piomelli 2011) in Figure 5. The profiles are extracted at equal distances from the dune crest, *i.e.*, at constant values of $x - x_s$, where $x_s = A\sin(2\pi z/\lambda)$ is the crestline shape. The flow over the saddle is similar to that in 2D

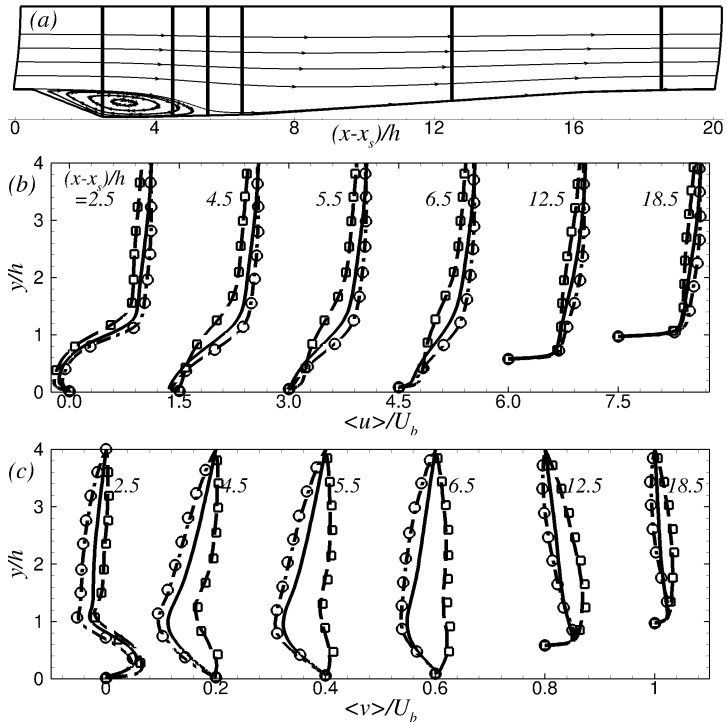

FIGURE 5. Dune geometry *(a)*, and profiles of the mean streamwise *(b)* and vertical *(c)* velocities at the locations shown in *(a)*, from left to right: $(x - x_s)/h$ = 2.5, 4.5, 5.5, 6.5, 12.5, 18.5. Case 5. ——— 2D dune; — — — lobe plane; —·—·— saddle plane. Symbols represent the simulation with a higher resolution with $384 \times 128 \times 384$ grid points; □ lobe plane; ◯ saddle plane. Each profile is shifted to the right for clarity. The mean-flow streamlines for a 2D dune are illustrated in *(a)* to aide the discussion.

dune, but with a higher speed. Over the lobe, the behaviour is similar in the recirculation region, but is significantly different further downstream, due to the 3D behaviour near the reattachment point. At $(x-x_s)/h = 6.5$, for instance, profiles of mean velocities have a two-layer shape in which the wake of the separated-shear layer lies above the internal boundary layer. The internal layer results in a local near-wall velocity maximum that persists throughout the stoss side, and generates an inflection point in the velocity profile that is not present in the 2D case, which may be responsible for the increased turbulent activity in the lobe planes (see below).

Profiles of mean vertical velocity (Figure 5*(c)*) show significant deviation from the 2D behaviour especially in the lobe plane; over the saddle, the downward motion of the fluid is somewhat faster (but the shape of the profile is unchanged), while over the lobe the flow is generally directed upwards, due to the displacement of the separated flow from the crest by the laterally moving fluid coming from the saddle and node region. While the streamwise velocity approaches the 2D behaviour over the downstream half of the stoss side, the vertical component does not.

Streamwise velocity profiles in wall units on the stoss side are compared to the 2D dune case in Figure 6. The velocity and the length are normalized with the viscosity and the local friction velocity, $u_{\tau,x} = (\tau_{w,x}/\rho)^{1/2}$, where

$$\tau_{w,x} = \frac{1}{Re}\frac{\partial\langle U\rangle}{\partial n}, \tag{3.1}$$

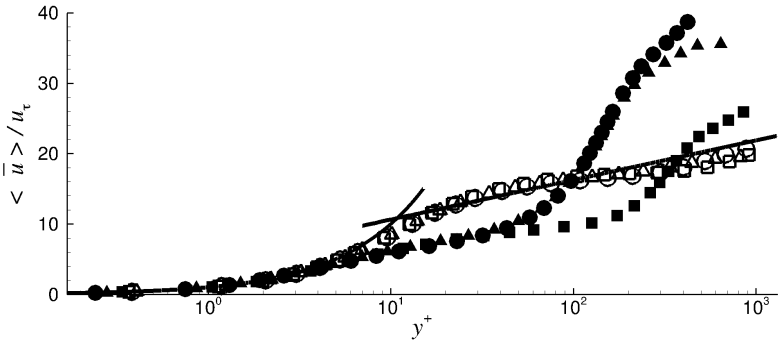

FIGURE 6. Mean streamwise-velocity profiles in wall units at $(x - x_s)/h = 6.5$ (filled symbols) and $(x - x_s)/h = 18.5$ (open symbols). ●, ○ 2D dune, ■,□ lobe plane, and ▲,△ saddle plane. The black solid lines represent the law-of-the-wall, $u^+ = y^+$ and $u^+ = \ln y^+/\kappa + 5.0$, with $\kappa = 0.41$.

and viscosity ν. Note that, since the simulations resolve the wall layer, the wall stress can be computed directly, and no approximation or extrapolation is needed. An inflection point in all profiles indicates the presence of a non-equilibrium boundary layer after reattachment. At $(x - x_s)/h = 6.5$, as observed above, the flow over the lobe deviates more significantly from 2D behaviour than that over the saddle. The profiles are characteristic of flows in strong adverse pressure-gradients, as also observed by Le *et al.* (1997) in the simulation of turbulent flow over a backward-facing step, and by Spalart & Watmuff (1993) in flat-plate boundary layers with pressure gradients. The adverse pressure-gradient is generated in the first half of the channel by the sudden flow expansion at the crest. Along the stoss side of dunes, the boundary layer develops faster over the lobe and at $(x-x_s)/h = 18.5$ all profiles collapse on the two-dimensional dune profile.

Figure 7 shows contours of the streamwise component of the wall stress, for five selected cases. The dashed white lines highlight the $\tau_{w,x} = 0$ contour. First, we note that longitudinal regions of low wall stress can be observed in all cases. In the first two cases (Figures 7*(a)* and *(b)*) they are aligned with the lobe, and are due to pairs of streamwise vortices, which advect low-speed fluid close to the bed towards the lobe and high-speed fluid from the outer flow towards the wall, thereby decreasing τ_w at the lobe and increasing it at the saddle. These vortices can be observed in Figure 8*(a)*. In Case 9 (Figure 7*(d)*), on the other hand, the streaks are due to a streamline convergence caused by the bottom topography; in case 10, two pair of vortices are present, one generated at the lobe, the other at the lobe on the upstream dune; Cases 9 and 10 will be discussed at length later. Case 8, Figure 7*(c)*, has a behaviour intermediate between Cases 1-8 and Case 9, including both the streaks due to the streamwise vortices and those due to the streamline convergence.

Case 9 has the lowest crestline wavelength, and different mean-flow characteristics. As Figure 9*(b)* illustrates, the streamwise velocity does not vary much in the spanwise direction. The typical secondary flow with large streamwise vortices between the lobe and the saddle, observed in the other cases, is not observed here (Figure 8*(b)*). In the channel interior, the spanwise velocity is negligible compared to the vertical one, and the flow characteristics are similar to the 2D dunes (Omidyeganeh & Piomelli 2011), as fluid moves downward in the first half of the channel and upward in the second half. Nezu & Nakagawa (1993) pointed out that large secondary currents similar to those observed in Cases 1-8 (Figure 3*(b)*) occur when the wavelength of the bed deformations in the spanwise direction is more than twice the flow depth; in Case 9 the wavelength

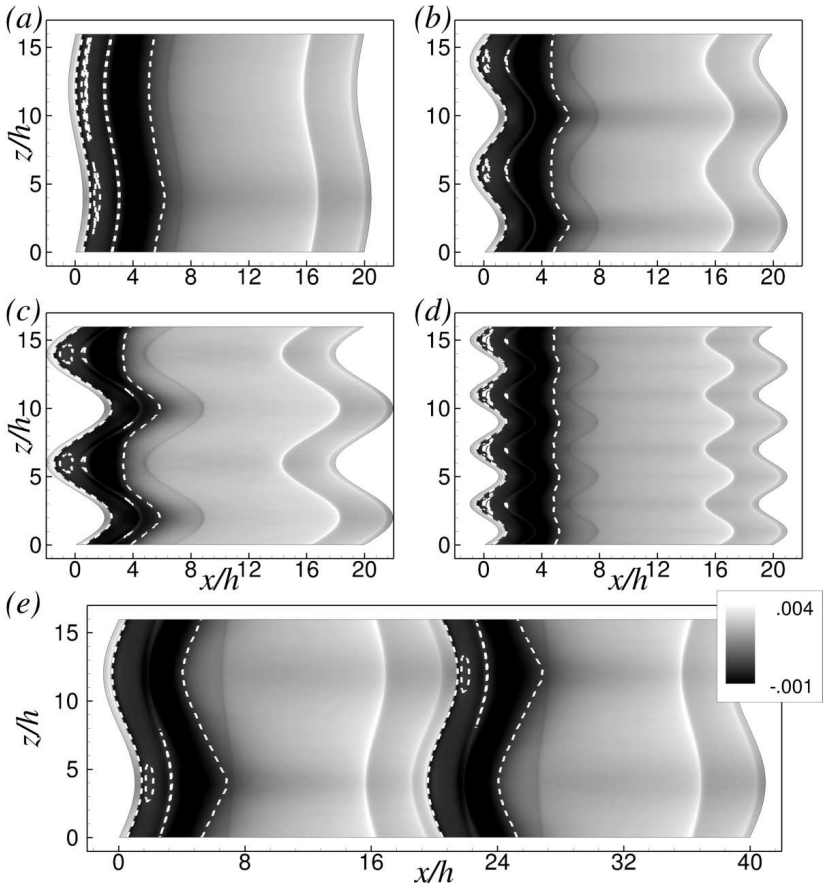

FIGURE 7. Contours of the streamwise component of the wall stress, $\tau_{w,x}/\rho U_b^2$. The dashed white lines highlight the $\tau_{w,x} = 0$ contour. *(a)* Case 2 ($\lambda = 16h$, NDS=1.04; *(b)* Case 5 ($\lambda = 8h$, NDS=1.14); *(c)* Case 8 ($\lambda = 8h$, NDS=1.46); *(d)* Case 9 ($\lambda = 4h$, NDS=1.46); *(e)* Case 10 ($\lambda = 16h$, NDS=1.14, staggered dunes).

is equal to the maximum flow depth ($\lambda = 4h$), and large-scale streamwise vortices are not observed. Although the streamwise vorticity in the interior of the channel is small compared to Cases 1–8 and 10, near the bed, due to the significant waviness of the bed in the spanwise direction, spanwise pressure gradient becomes significant and drives high-momentum fluid toward the lobe (Figure 10), causes a local high pressure zone at the lobe and low wall-shear stress stripes along the saddle plane in Figure 7*(d)*.

In Case 10, because of the staggered lobes and saddles, the flow develops quite differently (Figures 8*(c)* and 9*(c)*). First, as was also observed experimentally (Figure 6 in Maddux *et al.* (2003*a*,*b*)), the flow is faster over the node plane (Figure 9*(c)*). The near-bed streamlines shown in Figure 11 are qualitatively different than in Cases 1-8 (Figure 4), due to the different pressure distribution on the bed: the highest pressure is in the reattachment region over the node. The main difference in the streamlines occur on the stoss side of the saddle plane where they bend back toward the saddle. After the reattachment on the stoss side (*e.g.*, in the vertical planes at $x/h = 7$, 12, and 17 in Figures 8*(c)*), two strong vorticity contours with opposite signs are observed near the lobe. These vortices have a similar nature as those for Case 5 (Figure 8*(a)*). The vorticity contours decay as they travel over the saddle plane of the following dune. They can

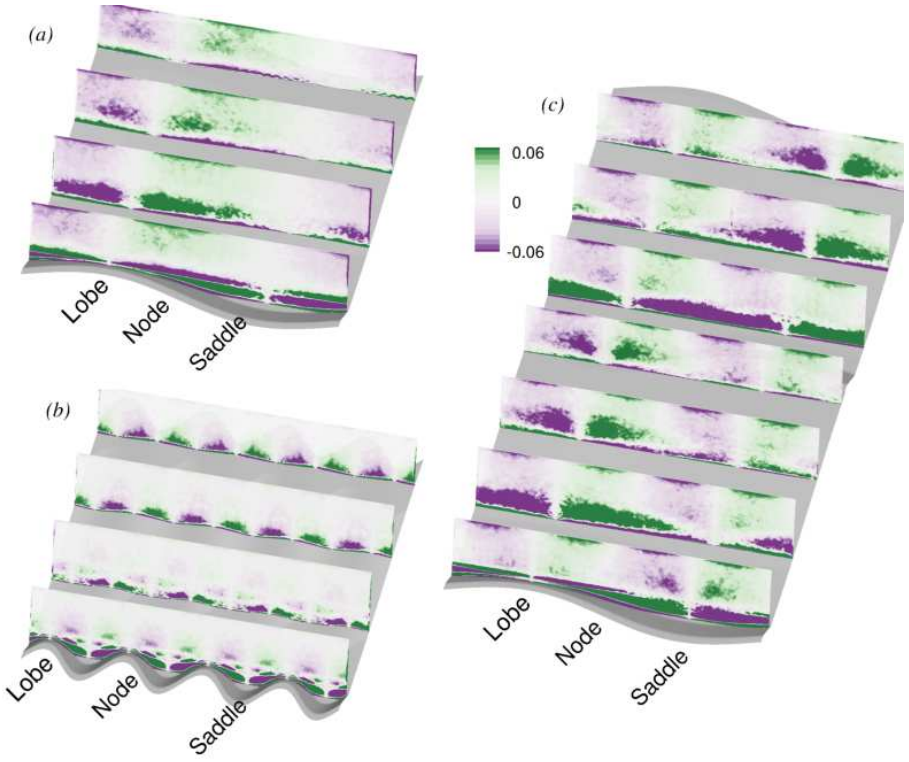

FIGURE 8. Contours of mean streamwise vorticity, $\Omega_x h/U_b$. *(a)* Case 1; *(b)* Case 9; *(c)* Case 10.

still be observed in the vertical plane at $x/h = 7$ in Figure 8*(c)*, and in the wall-stress contours in Figure 7*(e)*.

In Figure 7 we also observe secondary recirculation bubbles (similar to those occurring in backward-facing steps and in 2D dunes) over the lee face, in cases with low crest curvature. When the three-dimensionality is significant, however, the secondary recirculation zone is confined to the saddle region for Cases 1 to 9 and to the lobe for Case 10. The acceleration parameter

$$K = \frac{\nu}{U_\infty^2}\frac{dU_\infty}{dx}, \tag{3.2}$$

is negative in the the adverse-pressure gradient region over the lee side of the dune where the flow expands (Figures 12*(a)* and *(b)*). On the lobe plane, the deceleration is higher in Cases 1 to 9 than in Case 10 (which has staggered crestlines); hence, the streamlines diverge less over the lee side of Case 10 where a secondary recirculation is generated. The tangent of the angle of the streamlines over the crest, $\tan^{-1}(V/U)$, shown in Figure 12*(c)* is highest in Case 10 where the secondary recirculation disappears. The flow over the saddle plane in Case 10 (Figure 12*(d)*) slows down more, resulting in higher divergence of streamlines over the crest, and the generation of a secondary recirculation over the lee side is inhibited.

The position of the reattachment point is heavily influenced by the bedform geometry. For cases in which the dune crest is not highly 3D (typically, for $NDS = 1.01 - 1.05$), the reattachment line follows the shape of the dune crest (Figure 7*(a)* and *(b)*). As the three-dimensionality becomes more pronounced, the reattachment line becomes a

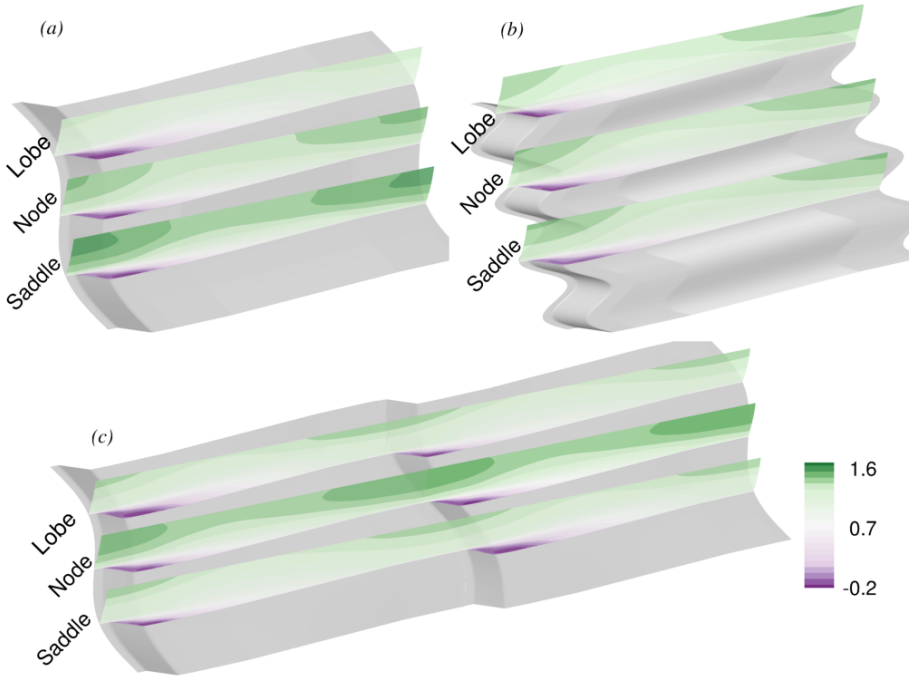

FIGURE 9. Contours of mean streamwise velocity, U/U_b. *(a)* Case 1; *(b)* Case 9; *(c)* Case 10.

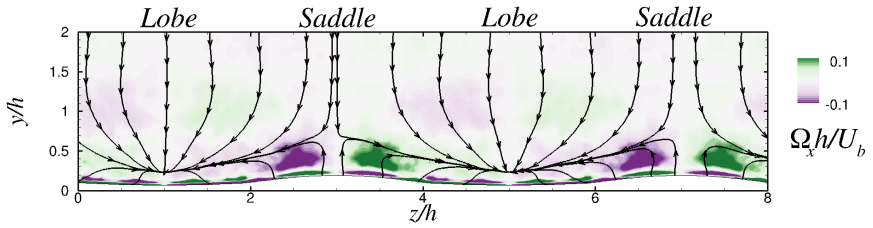

FIGURE 10. Mean-flow streamlines tangential to the cross plane at $x/h = 7$ and mean streamwise vorticity contours, $\Omega_x h/U_b$, for Case 9.

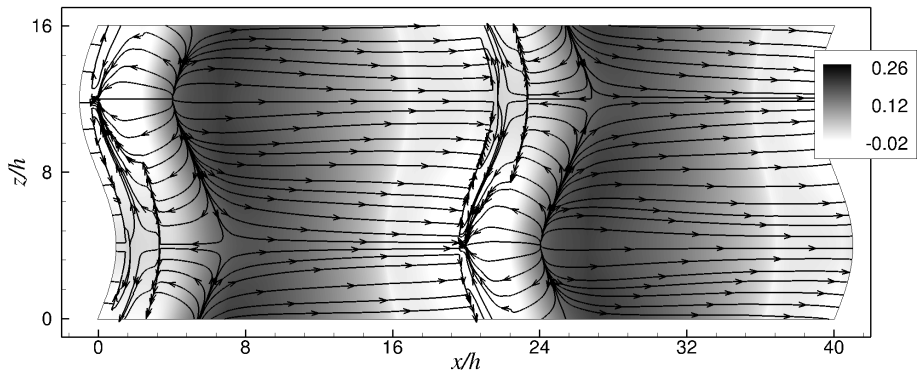

FIGURE 11. Mean-flow streamlines and mean pressure contours, $\overline{P}/U_b^2$, on a plane near the bed ($y^+ \approx 3$) for Case 10.

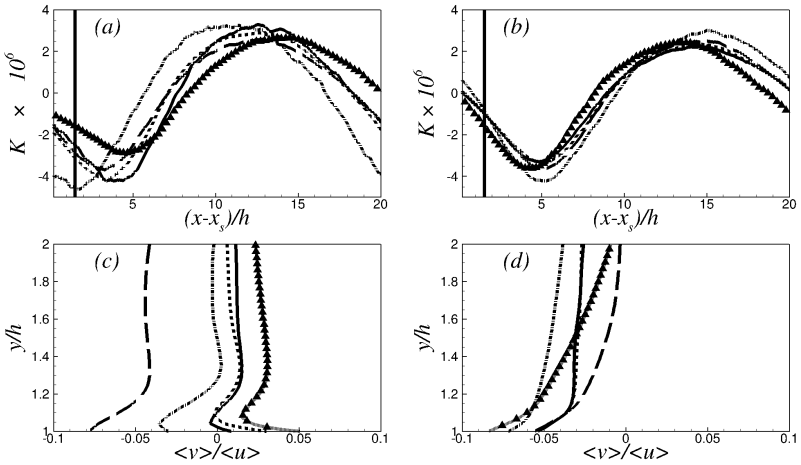

FIGURE 12. Acceleration parameter (Equation 3.2) over *(a)* the lobe and *(b)* the saddle. Tangent of the angle of streamlines with respect to the x-axis at $(x - x_s)/h = 1.5$ over *(c)* the lobe and *(d)* the saddle. ——— Case 2; - - - Case 5; —·—·— Case 8; ——— Case 9; ▲ Case 10.

deformed sinusoid, indicating that the shear layer vortices and the secondary flow play a significant role.

The reattachment length (as a function of spanwise distance z, normalized by the wavelength λ) is shown in Figure 13 for all cases. The lobe and saddle planes are at $z/\lambda = 0.25$ and 0.75, respectively. We observe several features of interest. First, in most cases the distance to reattachment is longer in the saddle plane than in the lobe plane. This may be due to the higher momentum of the fluid over the saddle. In most cases we also observe a bulge in the reattachment length over the lobes, caused by the secondary flow near the bed in which fluid moves from the saddle towards the lobe and inhibits the reattachment of mean flow on the stoss side. The bulging effect is more pronounced for intermediate values of the NDS (in the range 1.04-1.21), then decreases, to disappear completely in Case 9 (short wavelength). The case with staggered dunes also has a different behaviour, where reattachment occurs earlier over the saddle plane than over the lobe due to lower deceleration in the saddle plane (Figure 12*(a)* and *(b)*), which forces the reattachment of the flow. The bulging effect disappears over the lobe plane. As discussed, the secondary flow patterns differ in the last two cases, and the lack of secondary flow is the primary cause for the different recirculation regions. The bedform three-dimensionality tends to decrease the reattachment length (Figure 14), mostly through the secondary flow. The effect of the crestline wavelength on the average reattachment length is not significant.

3.2. *Channel resistance*

Contours of the streamwise component of the wall-shear stress in Cases 1–8 (Figure 7) show that the flow over the saddle plane has the highest mean velocity, and that the maximum shear stress on the bed occurs over the stoss side of the saddle plane. The wall-shear stress becomes negative immediately downstream of the crestline. Note the localized jumps in the contours that correspond to discontinuities in the slope of the dune. Except near the lobe, the wall-shear stress on the stoss side, after reattachment, is almost uniform in the spanwise direction. After the reattachment line in Case 9, the wall-shear stress is almost uniform due to the fact that the secondary flow is weak (Figure 8*(b)*) and cannot deform the distribution of the attached flow. Case 10 has the highest wall-shear stress between the saddle and the lobe planes, which is consistent with the

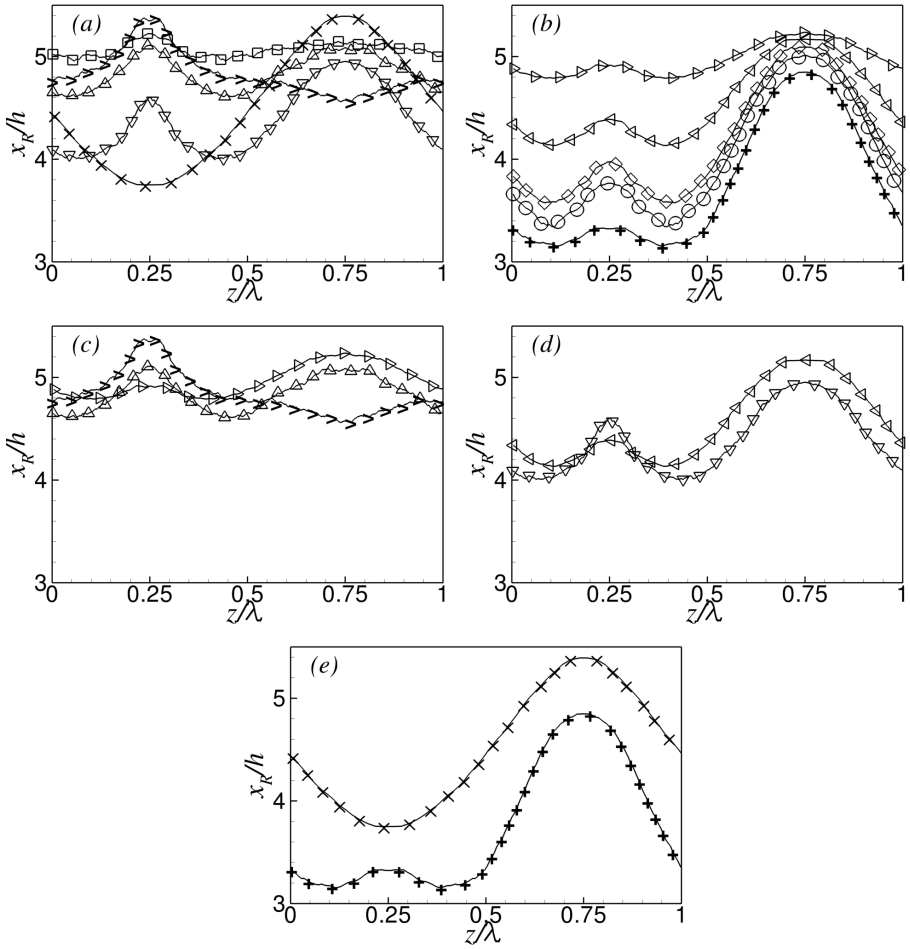

FIGURE 13. Reattachment length. □, Case 1; △, Case 2; ▽, Case 3; ▷, Case 4; ◁, Case 5; ◊, Case 6; ◯, Case 7; +, Case 8; ×, Case 9; >, Case 10. *(a)* Cases 1, 2, 3, 10 ($\lambda = 16h$) and 9 ($\lambda = 4h$) ; *(b)* Cases 4 through 8 ($\lambda = 8h$); *(c)* Cases 2, 4 and 10 (NDS=1.04, $\lambda = 16h$, $8h$ and $16h$ with staggered dunes; *(d)* Cases 3 and 5 (NDS=1.14, $\lambda = 16h$ and $8h$); *(e)* Cases 8 and 9 (NDS=1.46, $\lambda = 8h$ and $4h$).

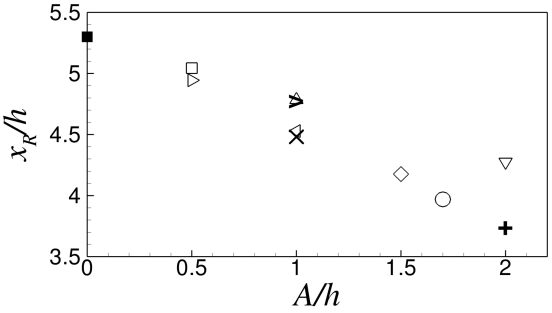

FIGURE 14. Average reattachment length. ■, 2D case (Omidyeganeh & Piomelli 2011); □, Case 1; △, Case 2; ▽, Case 3; ▷, Case 4; ◁, Case 5; ◊, Case 6; ◯, Case 7; +, Case 8; ×, Case 9; >, Case 10.

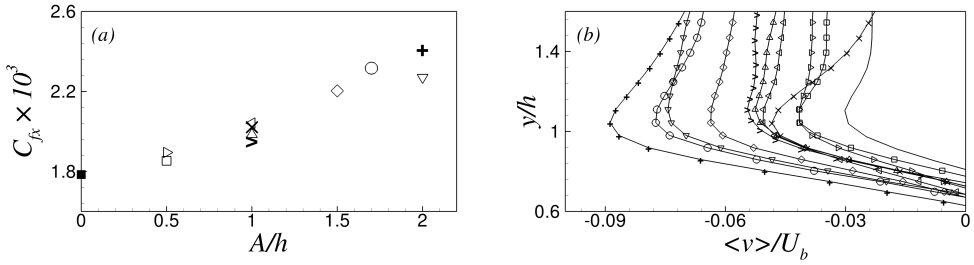

FIGURE 15. *(a)* Average streamwise skin-friction coefficient. *(b)* Mean-vertical velocity component at $(x-x_s)/h = 2.5$ near the separated streamlines over the saddle. ■, 2D case (Omidyeganeh & Piomelli 2011); □, Case 1; △, Case 2; ▽, Case 3; ▷, Case 4; ◁, Case 5; ◊, Case 6; ◯, Case 7; +, Case 8; ×, Case 9; >, Case 10; solid line without symbol is for 2D case.

observation by Maddux *et al.* (2003*a*,*b*) that the depth-averaged streamwise velocity is maximum over the node plane (Figure 6 in their article).

Spanwise variation of the skin friction results in a different bed-load sediment transport rate along the width of the channel; as indicated by Kostaschuk & Villard (1996), when the wall-shear stress is low, less sediment transport occurs, and the decreased suspension of sediment results in more asymmetric dune geometries, with steeper lee side. Considering these facts, the present results can be useful for a sediment transport investigation that uses mathematical models to predict bed deformations.

From the distribution of the wall-shear stress, the average skin-friction coefficient in the streamwise direction (Figure 15*(a)*) can be computed:

$$C_{f,x} = \frac{\int_{bed} \tau_{w,x}\, ds}{L \times W \times \frac{1}{2}\rho U_b^2}, \tag{3.3}$$

where $\tau_{w,x}$ is the streamwise component of the wall-shear stress, $L = 20h$ is the dune wavelength in the streamwise direction, and $W = 16h$ is the width of the domain. The streamwise skin-friction coefficient increases monotonically with the amplitude A (Figure 15*(a)*), but does not depend strongly on the wavelength or the NDS coefficient. Cases with higher crestline amplitude have stronger downwash of fast flow toward the bed over the lee side of the saddle plane (Figure 15*(b)*), which increases the skin friction. Sirovich & Karlsson (1997) showed that the skin friction decreases if the arrangement of the roughness elements on the bed is random; any systematic arrangements increases the friction.

The average spanwise skin friction is zero by symmetry, since the spanwise wall stress between a saddle and the next lobe is opposite in sign to the stress from that lobe to the next saddle. Although zero in the mean, the effect of the spanwise component of the wall stress is to contribute to the decay of large (especially streamwise) vortices and to the transport of sediment in the spanwise direction; we computed the magnitude of the spanwise skin-friction coefficient from a saddle plane to the next lobe plane and multiplied it by twice the number of waves in the domain, to obtain a measure of the spanwise force acting on the flow locally. The result is illustrated in Figure 16*(a)*. The spanwise skin-friction coefficient is at most 10% of the streamwise counterpart, and increases with amplitude A, like the streamwise skin-friction coefficient. The maximum spanwise wall-shear stress occurs in the lee side, and is directed from the saddle plane to the lobe plane by pressure gradient. Note that the spanwise wall stress in Case 9 is negligible, due to the absence of secondary flow. In the case of staggered crestlines (Case 10), the flow is

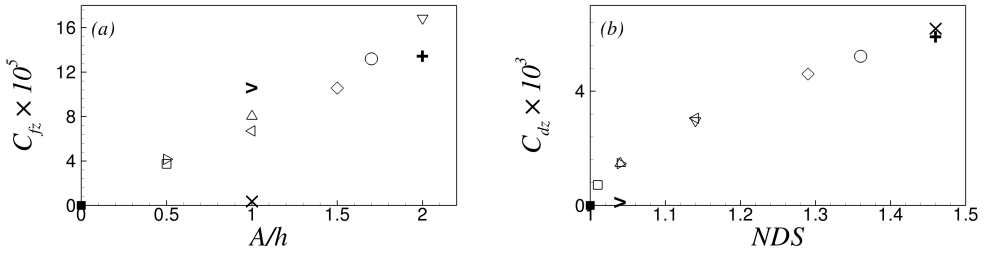

FIGURE 16. Average spanwise *(a)* skin-friction and *(b)* form-drag coefficients. ■, 2D case (Omidyeganeh & Piomelli 2011); □, Case 1; △, Case 2; ▽, Case 3; ▷, Case 4; ◁, Case 5; ◊, Case 6; ◯, Case 7; +, Case 8; ×, Case 9; >, Case 10.

faster between the lobe and the saddle planes, where the spanwise wall-shear stress is significant; hence the stress is larger than in other cases with the same crestline amplitude (Cases 2 and 5).

The form drag is computed by integrating the pressure force on the bed and is directly related to the difference between the high pressure on the stoss side and low pressure on the lee side, as well as the area of the bed that faces the streamwise or spanwise directions. For high crestline amplitudes, the pressure on the stoss side of the saddle plane is high, due to the fact that the flow has higher momentum, but the pressure on the stoss side of the lobe plane is low. This is a first-order effect, and the details of the crestline shape do not seem to affect the results much: the form-drag coefficient in the various cases differs by less than 7%, ranges from 5.6×10^{-3} to 6.1×10^{-3} while for the 2D case it is equal to 5.7×10^{-3} (Omidyeganeh & Piomelli 2011).

The introduction of the 3D crestline increases the spanwise form drag from the lobe to the next saddle plane, as the pressure gradient increases in the spanwise direction. Similar to the spanwise skin-friction coefficient, we compute the magnitude of the spanwise form-drag coefficient from a saddle plane to the next lobe plane and multiply it by twice the number of waves in the domain, to obtain a measure of the spanwise force that, in real flows, would contribute to deformation of the crestline. The spanwise form drag, shown in Figure 16*(b)*, depends strongly on the curvature of the crestline, and increases with curvature, to approach the streamwise form drag in Cases 8 and 9. Except for Case 10, we observe a monotonic increase of the form drag as NDS increases (*i.e.*, as the spanwise component of the lee-side face increases). The low value of $C_{d,z}$ in the case of staggered crestlines is caused by a major difference in the bedform of Case 10, as the normal vector of bed surface on the stoss side has a small component in the spanwise direction; the dune wavelength is varied in the spanwise direction ($18h$ over the lobe plane, $20h$ over the node plane, and $22h$ over the saddle plane) to accommodate the staggered crestlines, hence the contribution of the pressure force on the stoss side to the spanwise form drag decreases significantly.

The streamwise channel resistance (the skin friction plus the form drag) is a function of the crestline amplitude, A, while the spanwise channel resistance is a function of the curvature and the amplitude of the crestline. The total spanwise resistance can reach 76% of the streamwise resistance at high amplitude and curvature (Case 8), where the spanwise form drag and friction adds up to 6.1×10^{-3} (Figure 16), while the streamwise counterpart is 8.1×10^{-3} (Figure 15).

Form drag contributes more than 70% to the channel resistance (Figure 17); this contribution increases with the crestline curvature, NDS. For any wavelength, there seems to be an asymptotic value for this contribution that increases for lower wavelengths λ,

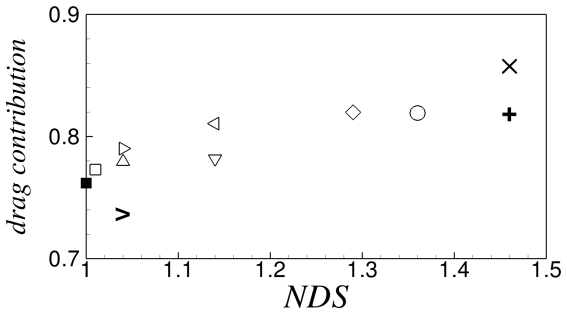

FIGURE 17. Average drag contribution into the channel resistance (form drag/total resistance). ■, 2D case (Omidyeganeh & Piomelli 2011); □, Case 1; △, Case 2; ▽, Case 3; ▷, Case 4; ◁, Case 5; ◊, Case 6; ◯, Case 7; +, Case 8; ×, Case 9; >, Case 10.

up to a value of 86% for Case 9. Case 10 shows a significant decrease of the relative importance of form drag, due to the high skin friction and the low form drag (comparable with the 2D case) which was discussed before and shown in Figures 15*(a)* and 16.

3.3. *Reynolds stresses*

As is the case in many flows with massive separation, the flow over the dunes is critically affected by the shear layer that forms at separation. In 3D dunes, the modulation of the crestline causes the shear-layer height to vary along the span. As the turbulence production is very large in this region, this modulation affects the Reynolds stresses significantly. Figure 18 shows contours of the turbulent kinetic energy (TKE), $q^2/2$, where $q^2 = \langle u_i' u_i' \rangle$ is the trace of the Reynolds stress tensor, a prime represents the fluctuating part of the resolved velocity field, and $\langle \cdot \rangle$ represents the average in time and about the symmetry (or anti-symmetry) lobe and saddle planes for three representative cases (Cases 5, 9 and 10). The proper symmetries are considered to increase statistical samples.

In Case 5, which is representative of most of the configurations studied, the TKE is highest along the separated-shear layer after the crestline (Figure 18*(a,b)*). Compared to 2D dunes, the TKE in the separated-shear layer is suppressed over the saddle by the high-momentum fluid that converges on this plane and moves downward to the bed, and increased in the lobe plane by the upward movement of low-momentum fluid advected from the near-wall flow. The height of the separated-shear layer varies in the spanwise direction (Figure 18*(b)*). Over the lobe, the shear layer is lifted towards the top surface more than in the saddle plane. Contours are uniform in the spanwise direction except around the lobe.

Instantaneous vortical structures, visualized by contours of spanwise and streamwise vorticity, are shown in Figures 20*(a)* and *(b)* for Case 5. Most of the structures are observed in the separated-shear layer, around the reattachment region, and near the wall on the stoss side of the dune. In the saddle plane, vortical structures generated at the crestline due to the Kelvin-Helmholtz instability are advected downstream towards the reattachment region on the bed where they interact with the wall turbulence. In the lobe plane, vortical structures extend vertically in a broader range as they are advected downstream in the separated-shear layer. This is consistent with time-averaged statistics shown in Figure 19 that indicate that the shear layer is wider and has a maximum Reynolds stress at a higher distance from the bed. Coherent structures in the node plane in the separated-shear layer have the same characteristics as those in the saddle and

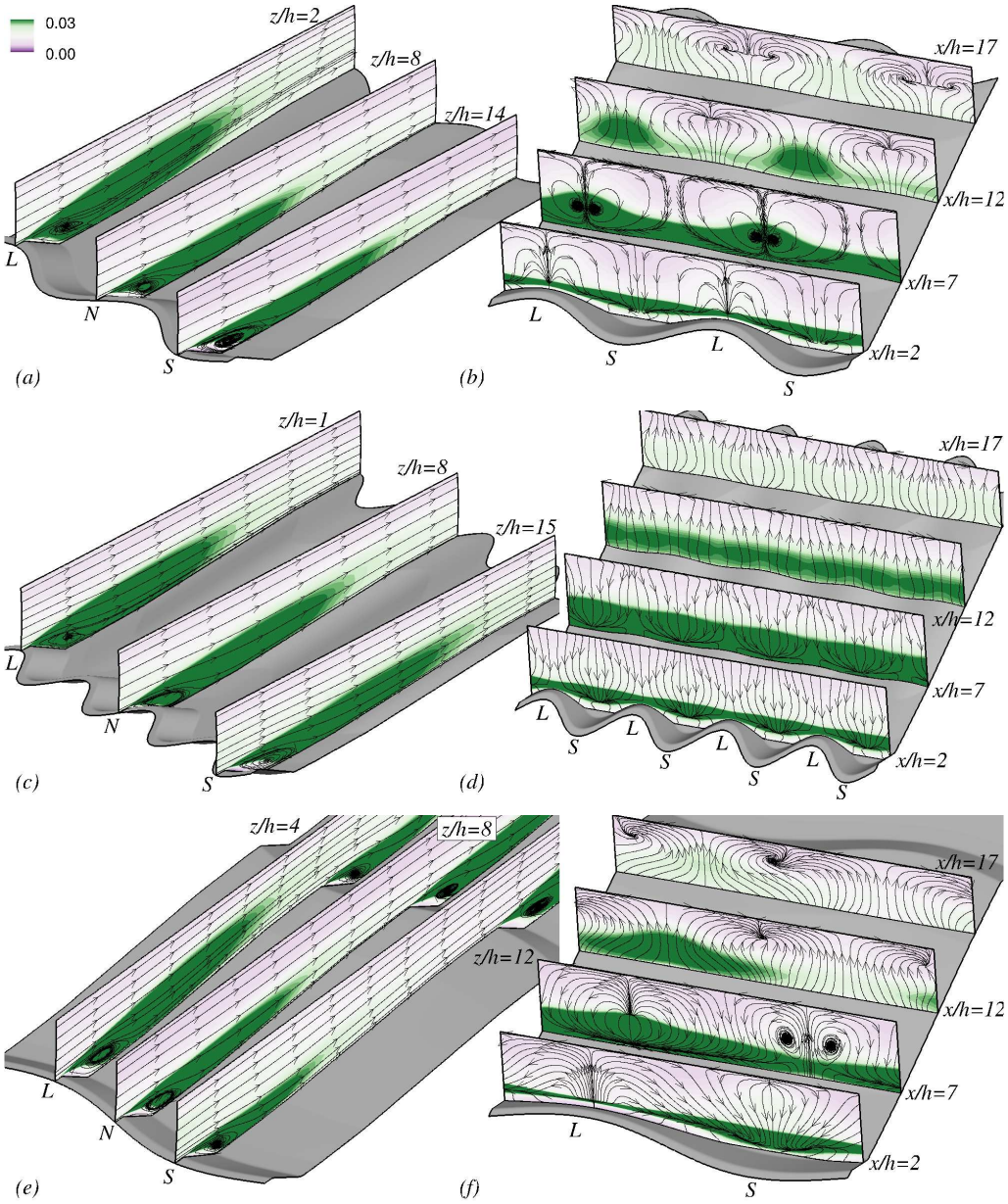

FIGURE 18. Contours of mean-turbulent kinetic energy $q^2/2 = \langle u_i' u_i' \rangle / 2U_b^2$ on three vertical planes on the lobe, the node, and the saddle planes (*a,c,e*), and four vertical planes at $x/h = 2, 7, 12, 17$ (*b,d,f*) for *(a,b)* Case 5, *(c,d)* Case 9, and *(e,f)* Case 10; streamlines of mean flow are shown on these planes.

the lobe planes, although the near-bed structures are significantly more numerous there than close to the reattachment region. This is explained by the spanwise-directed flow in this region that advects the near-bed structures from the saddle plane toward the lobe plane. The instability of the separated-shear layer is shown in Figure 20*(b)*: on the vertical plane $x/h = 2$, most of the structures are concentrated in the recirculation region. Some structures are advected from the upstream dune and are observed above

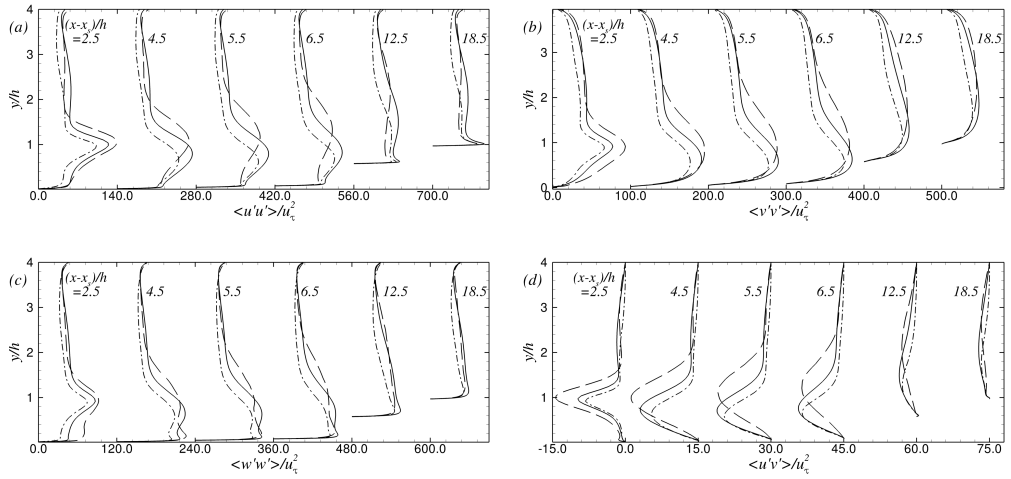

FIGURE 19. Profiles of Reynolds stresses normalized by $u_{\tau,x}^2$ for Case 5. *(a)* $\langle u'u' \rangle$; *(b)* $\langle v'v' \rangle$; *(v)* $\langle w'w' \rangle$; *(d)* $\langle u'v' \rangle$. The position of the profiles is the same as in Figure 5; $x_s = A\sin(2\pi z/\lambda)$ is the crestline position; each profile is shifted to the right for clarity. ——— 2D dune; — — — lobe plane; —·—·— saddle plane.

the shear layer. At a position further downstream, $x/h = 12$, after flow reattachment on the stoss side of the bed, an interaction of vortical structures with the wall turbulence is observed and we are unable to distinguish the shear layers anymore. Although vortical structures occupy almost the whole flow depth over the lobe and its neighbourhood, at this distance downstream of the crestline the structures are mixed more across the channel width. The quantitative and qualitative analyses of coherent structures require comprehensive studies of all different cases and this will be presented in a follow-up article.

The lack of secondary flow in Case 9 results in a uniform spanwise distribution of TKE, Figure 18*(d)*, although the TKE is higher than in the 2D case (Omidyeganeh & Piomelli 2011). The staggering of the crestlines in Case 10 alters the secondary flow observed in Cases 1–8. The near-bed flow from the saddle plane to the lobe plane is still effective, but the mean flow reattaches on the stoss side over the lobe plane, while it does not in Cases 1–8; at $x/h = 7$, for instance, the mean flow near the bed is directed downward in Case 10 (Figure 18*(f)*) and upward in Case 5 (Figure 18*(b)*). As a result, the separated shear-layer is not raised towards the top surface as much as in Case 5. At $x/h = 12$ and 17, the near-bed flow from the saddle plane toward the lobe plane and larger vertical velocity over the lobe increases the TKE over the lobe (Figure 18*(f)*). Away from the bed and above the separated shear-layer the TKE is high in the saddle plane over the lee side ($x/h = 2$) since the upstream shear layer is advected from the lobe plane (Figure 18*(e)*) that reaches the downstream saddle plane.

Reynolds-stress profiles (normalized by $u_{\tau,x}^2 = \tau_{w,x}/\rho$) in the lobe and saddle planes of Case 5 are shown in Figure 19. The secondary shear stresses, $\langle u'w' \rangle$ and $\langle v'w' \rangle$, are zero on these symmetry planes and not shown here. In the saddle plane, the profiles follow the 2D behaviour, although their magnitudes are lower due to the secondary flow, which advects high-momentum fluid toward the bed; while over the lobe the normal stresses are larger near the crest, $(x - x_s)/h = 2.5$, and the peak occurs at a higher elevation, following the behaviour of the separated-shear layer. Higher TKE in the separated-shear layer over the lobe may be explained by a value of the acceleration parameter over the lee

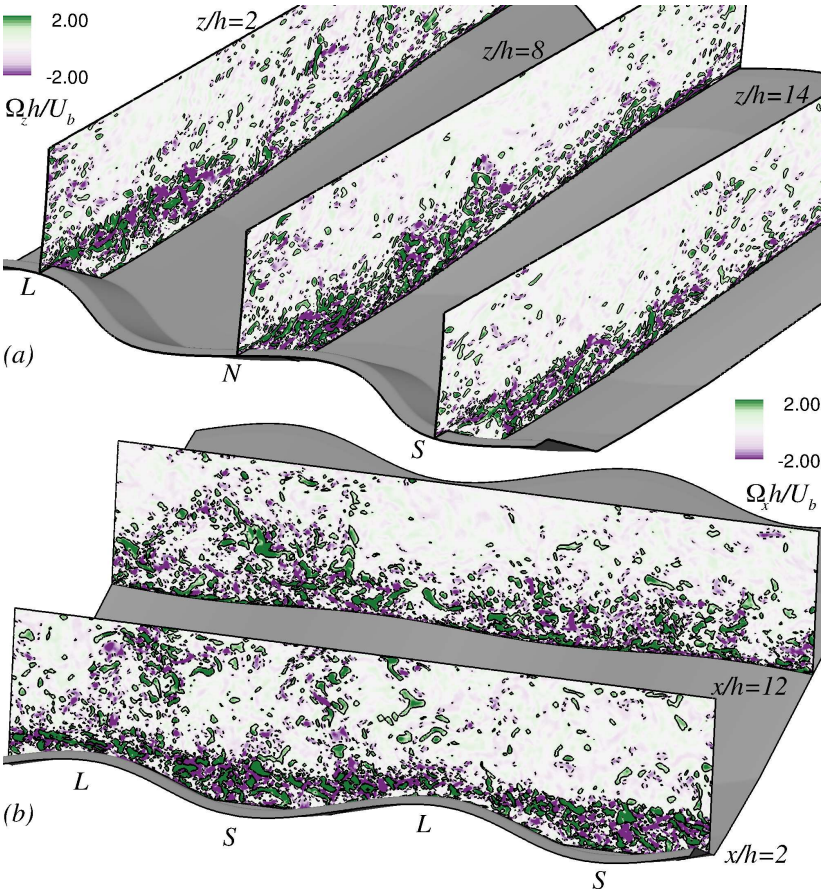

FIGURE 20. Case 5. *(a)* Instantaneous spanwise vorticity contours on three $xy-$planes, and *(b)* instantaneous streamwise vorticity contours on two $yz-$planes. ——— , U_b/h; - - - $-U_b/h$

side of that is 24% smaller than in the saddle plane; the peak values of Reynolds-normal stresses and Reynolds shear stress are also approximately $8-20\%$ and 50% respectively higher than the value those in the saddle plane at this position. At a higher deceleration, the shear layer over the lobe becomes broader and is lifted toward the top surface by the upward moving of the mean flow. An internal boundary layer is developed after the reattachment on the stoss side of dunes (Kostaschuk & Church 1993; Best *et al.* 2001; Nelson *et al.* 1993; Kadota & Nezu 1999; Bennett & Best 1995; Venditti & Bennett 2000; Balachandar *et al.* 2007), which results in a near-wall peak of the normal stresses in Figure 19*(a,c)*. The internal boundary layer has higher streamwise stressess in the saddle plane, since the local Reynolds number is higher; however, the spanwise stresses (Figure 19*(c)*) near the bed have a larger peak in the lobe plane due to the spanwise motion of the internal boundary layer. The physics of the near-wall flow have not been studied experimentally with the same detail as the present simulations; within these limits, however, the experimental observations (Maddux *et al.* 2003*a*,*b*; Venditti 2007), are qualitatively consistent with the current observations.

Because of the three dimensionality of the flow, the secondary stresses $\langle u'w' \rangle$ and $\langle v'w' \rangle$ are non-zero away from the symmetry planes. Since their contribution to the production of TKE is at least one order of magnitude smaller than that of the dominant terms, $\langle u'v' \rangle \partial U/\partial y$ and $\langle u'u' \rangle \partial U/\partial x$, they are not discussed here.

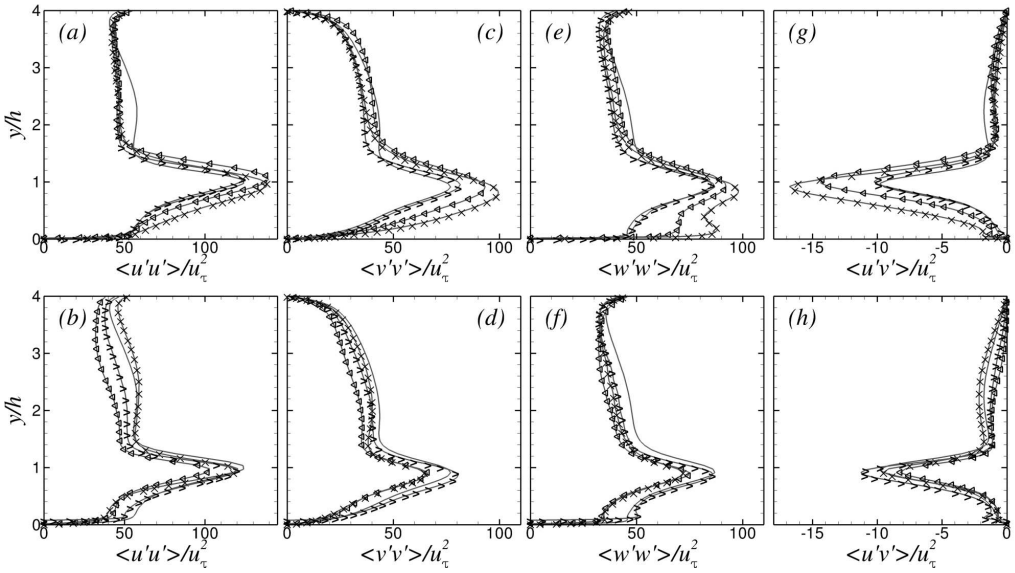

FIGURE 21. Average *(a,b)* streamwise Reynolds normal stress, *(c,d)* vertical Reynolds normal stress, *(e,f)* spanwise Reynolds normal stress, *(g,h)* Reynolds shear stress $\langle u'v' \rangle$, normalized by the spatially averaged wall-shear stress $u^2_{\tau,x}$, in the lobe *(a,c,e,g)* and saddle *(b,d,f,h)* planes at $(x - x_s)/h = 2.5$. Solid line without symbol is for the 2D case (Omidyeganeh & Piomelli 2011); $\lhd$, Case 5; $\times$, Case 9; $>$, Case 10.

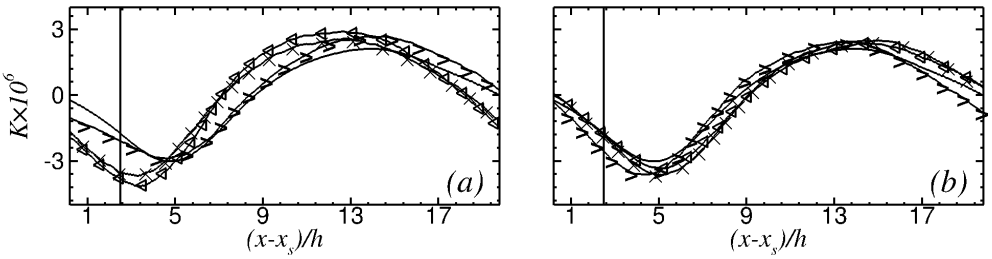

FIGURE 22. Acceleration parameter defined in 3.2, *(a)* over the lobe and *(b)* saddle planes. Solid line without symbol is for 2D case (Omidyeganeh & Piomelli 2011); $\lhd$, Case 5; $\times$, Case 9; $>$, Case 10. The vertical solid line represents the position of the profiles in Figure 21.

Profiles of the Reynolds stresses for Cases 5, 9 and 10 are compared over the lobe and the saddle planes at $(x - x_s)/h = 2$ with the 2D dune simulation (Omidyeganeh & Piomelli 2011) in Figure 21. The profiles are again normalized by the streamwise friction velocity. In the separated shear-layer the normal stresses and the shear stress $\langle u'v' \rangle$ have larger peaks in Cases 5 and 9 than in the 2D case, while Case 10 has an almost identical peak (Figure 21*(a,c,e,g)*). This behaviour is due to a larger negative value of the acceleration parameter in Cases 5 and 9 (Figure 22*(a)*), which enhances the instability of the separated shear-layer and increases the stresses. Case 9, with higher crest curvature than the other cases, presents higher turbulent stresses near the bed over the lobe plane, the 3D mixing of the backflow is expected to be stronger. On the other hand, over the saddle plane, the Reynolds stresses are smaller in the 3D cases than the 2D case and Case 10, which again is explained by a lower acceleration parameter compared to the other geometries (Figure 22*(b)*).

The peak above the separated shear-layer, $y/h \simeq 2.5$, which is due to the shear layer

generated by the upstream dune, is significantly damped in Cases 5 and 10 over the lobe plane (Figure 21*(a,g)*). The mixing in the vertical direction by the secondary flow, which flattens the profiles, is responsible for this phenomenon; as expected, this behaviour is nearly absent in Case 9, which has a very weak secondary flow.

4. Conclusions

Three-dimensional bedforms induce a 3D mean flow significantly different from the 2D case. The bedforms studied herein can be divided into three categories. First, Cases 1 to 8 (with in-phase crestlines and wavelength $\lambda \geq 8.0h$) have qualitatively similar behaviour in which low-momentum fluid near the bed moves away from the saddle toward the lobe, and then upwards towards the top surface; high-momentum fluid has the opposite motion. This secondary flow generates a pair of large streamwise vortices that straddle the lobe plane. Venditti (2007) also observed this secondary flow in his experiment. The near-wall motion displaces the separation line, and closes the recirculation bubble.

In Case 9, which has a very short wavelength (with in-phase crestlines), the near-bed characteristics are similar to the previous cases, but the interior flow is similar to that in 2D dunes. The absence of secondary flow in this case may be due to the fact that the wavelength of the crestline is smaller than the flow depth and the large secondary-flow vortices observed in the other cases do not fit between a lobe and a saddle. Finally, in Case 10 (in which the spanwise positions of the saddle and the lobe are staggered), the flow is affected by the staggering, which results in faster flow in the node plane rather than the saddle and the lobe planes. Maddux *et al.* (2003*b*) observed a similar behaviour in their experiments where the height of the crestline is altered with a sine wave. Two counter-rotating vortex pairs are observed; one straddling the lobe plane, similar to those in Cases 1-8, persists through the following dune, resulting in a second pair that straddles the saddle plane.

Near the bed, secondary flow is induced by the spanwise pressure gradient directed from the saddle toward the lobe. This motion displaces upwards the separated flow, which does not reattach on the bed. Therefore, the physics of the flow near the lobe plane are different from those in the rest of the domain. The reattachment length profile along the spanwise direction presents a bulge near the lobe, in which the reattachment length becomes larger than that of a corresponding 2D flow. This reattachment is due to the spanwise motion and not to the separated streamlines reaching the wall. The near-bed streamlines resemble those of Allen (1968), and the bulging effect is explained by the saddle point of separation caused by the 3D separation at the sinusoidal crestlines (Chapman & Yates 1991). The average value of the reattachment length is lower for 3D cases than the corresponding 2D case due to the effect of the streamwise vortices, which are correlated with the amplitude of the crestline.

The distribution of the wall-shear stress is almost uniform on the stoss side (its maximum occurs in the saddle plane in Cases 1–9 and in the node plane in Case 10) except in the lobe plane, where it is significantly lower. The average streamwise skin-friction coefficient increases monotonically as a function of the crestline amplitude due to a stronger downwash of high-speed flow toward the bed over the lee side that occurs for large crestline deformations. Although the average spanwise skin friction is zero due to the symmetry of the bed form, the spanwise wall stress contributes locally to transport of momentum and energy in the spanwise direction. A larger crestline deformation induces stronger spanwise motions and increases the local stress. The spanwise friction coefficient is negligible in Case 9, without the secondary flow (similar to the corresponding 2D dunes), while the staggering of the crestlines (Case 10), which causes the flow to be faster

in the node plane, results in increased friction, compared to non-staggered cases. The average streamwise form-drag coefficient does not change significantly among the cases. A local measure of the spanwise form-drag coefficient, on the other hand, correlates with the curvature of the crestline. The form drag contribution to the channel resistance (the skin friction plus the form drag) increases as a function of the curvature and reaches an asymptotic value, higher for smaller wavelengths.

The flow over dunes is affected by the separated shear-layer, in which the turbulent kinetic energy (TKE) is highest. The TKE is suppressed in the saddle plane due to convergence of the high-momentum fluid on this plane, and increased in the lobe plane due to a stronger deceleration of the flow on the lee side. Around the saddle points of separation in Cases 1-8 in the lobe planes, the separated-shear layer is raised toward the top surface. The internal boundary layer that is developed after the reattachment on the stoss side is higher $\langle u'u' \rangle$ in the saddle plane due to a higher local Reynolds number, while $\langle w'w' \rangle$ is higher in the lobe plane due to the spanwise motion of the near-wall layer towards this plane. The behaviour of the vertical profiles of the Reynolds stresses in the separated shear-layer in the different geometries was also examined. When the deceleration is larger, the separated vortices become more unstable; hence, the stresses are increased. Near the bed at higher crestline curvatures, the mixing of the backflow plays a significant role and increases the Reynolds stresses. The separated-shear layer from the upstream dune is damped significantly by the upward motion of flow over the lobe. The lack of a secondary flow in Case 9 results in a more persistent shear layer from the upstream dune and uniform spanwise distribution of the Reynolds stresses. In the case of the staggered crestlines, the separated-shear layer is not raised towards the top surface as much as in the non-staggered cases. The Reynolds stresses in the staggered case, at the separated-shear layer, are almost identical to the corresponding 2D dunes, but the advected-shear layer from the upstream dune is damped.

In a follow-up article, we will describe the instantaneous coherent structures that exist in the flow over the three-dimensional dunes studied here, especially Cases 5 and 10 that have significant differences in the mean-flow statistics. Qualitative and quantitative analyses of vortical structures will be provided to gain insight into the sediment-transport mechanisms in these 3D morphologies, and their differences with 2D, transverse-dune configurations. The contribution of large-scale flow structures to turbulent events such as boils at the top surface will be discussed.

Acknowledgments

This research was supported by the Natural Sciences and Engineering Research Council (NSERC) under the Discovery Grant program. The authors thank the High Performance Computing Virtual Laboratory (HPCVL), Queen's University site, for the computational support. MO acknowledges the partial support of NSERC under the Alexander Graham Bell Canada NSERC Scholarship Program. UP also acknowledges the support of the Canada Research Chairs Program.

REFERENCES

Allen, J.R.L. 1968 *Current ripples: their relation to patterns of water and sediment motion.* North-Holland Pub. Co.

Armenio, V. & Piomelli, U. 2000 A Lagrangian Mixed Subgrid-Scale Model in Generalized Coordinates. *Flow, Turb. Combust.* **65**, 51–81.

Ashley, G. M. 1990 Classification of large-scale subaqueous bedforms: a new look at an old problem. *J. Sedim. Petrol.* **60** (1), 160–172.

Baas, J. H. 1994 A flume study on the development and equilibrium morphology of current ripples in very fine sand. *Sedimentology* **41**, 185–209.

Baas, J. H. 1999 An empirical model for the development and equilibrium morphology of current ripples in fine sands. *Sedimentology* **46**, 123–138.

Baas, J. H., Oost, A. P., Sztano, O. K., de Boer, P. L. & Postma, G. 1993 Time as an independent variable for current ripples developing towards linguoid equilibrium morphology. *Terra Nova* **5**, 29–35.

Babakaiff, S. C. & Hickin, E. J. 1996 Coherent flow structures in squamish river estuary, british columbia, canada. In *Coherent Flow Structures in Open Channels* (ed. P. Ashworth, S.J. Bennett, J.L. Best & S.J. McLelland), pp. 321–342. Wiley.

Balachandar, R. & Patel, V. C. 2008 Flow over a fixed rough dune. *Can. J. Civ. Eng.* **35**, 511–520.

Balachandar, R., Yun, B.-S. & Patel, V. C. 2007 Effect of depth on flow over a fixed dune. *Can. J. Civ. Eng.* **43**, 1587–1599.

Bennett, S. J. & Best, J. L. 1995 Mean flow and turbulence structure over fixed, two-dimensional dunes: implications for sediment transport and bedform stability. *Sedimentology* **42**, 491–514.

Bennett, S. J. & Best, J. L. 1996 Mean flow and turbulence structure over fixed ripples and the ripple dune transition. In *Coherent Flow Structures in Open Channels* (ed. P. Ashworth, S.J. Bennett, J.L. Best & S.J. McLelland), pp. 281–304. Wiley.

Best, J. L. 2005 The fluid dynamics of river dunes: A review and some future research directions. *J. Geophys. Res.* **119** (F04S02), 1–21.

Best, J. L., Kostaschuk, R. A. & Villard, P. V. 2001 Quantitative visualization of flow fields associated with alluvial sand dunes: results from the laboratory and field using ultrasonic and acoustic Doppler anemometry. *J. Visualization* **4** (4), 373–381.

Carling, P. A., Gölz, E., Orr, H. G. & Radeki-Pawlik, A. 2000 The morphodynamics of fluvial sand dunes in the River Rhine, near Mainz, Germany. I. Sedimentology and morphology. *Sedimentology* **47**, 227–252.

Chapman, G. T. & Yates, L. A. 1991 Topology of flow separation on three-dimensional bodies. *Appl. Mech. Rev.* **44** (7), 329–345.

Flemming, B. W. 1978 Underwater sand dunes along the southeast african continental margin – observations and implications. *Marine Geology* **28**, 177–198.

Gabel, S. L. 1993 Geometry and kinematics of dunes during steady and unsteady flows in the Calamus River, Nebraska, USA. *Sedimentology* **40**, 237–269.

Germano, M., Piomelli, U., Moin, P. & Cabot, W. H. 1991 A dynamic subgrid-scale eddy viscosity model. *Phys. Fluids A* **3**, 1760–1765.

Grigoriadis, D. G. E., Balaras, E. & Dimas, A. A. 2009 Large-eddy simulations of unidirectional water flow over dunes. *J. Geophys. Res.* **114**.

Hyun, B. S., Balachandar, R., Yu, K. & Patel, V. C. 2003 Assessment of PIV to measure mean velocity and turbulence in open-channel flow. *Exp. Fluids* **35**, 262–267.

Jackson, R. G. 1976 Sedimentological and fluid-dynamic implications of the turbulent bursting phenomenon in geophysical flows. *J. Fluid Mech.* **77**, 531–560.

Jordan, S. A. 1999 A large-eddy simulation methodology in generalized curvilinear coordinates. *J. Comput. Phys.* **148** (2), 322–340.

Kadota, A. & Nezu, I. 1999 Three-dimensional structure of space-time correlation on coherent vortices generated behind dune crests. *J. Hydr. Res.* **37** (1), 59–80.

Kim, J. & Moin, P. 1985 Application of a fractional step method to incompressible Navier-Stokes equations. *J. Comput. Phys.* **59**, 308–323.

Kostaschuk, R. & Villard, P. 1996 Flow and sediment transport over large subaqueous dunes: Fraser River, Canada. *Sedimentology* **43**, 849–863.

Kostaschuk, R. A. 2000 A field study of turbulence and sediment dynamics over subaqueous dunes with flow separation. *Sedimentology* **47** (3), 519–531.

Kostaschuk, R. A. & Church, M. A. 1993 Macroturbulence generated by dunes: Fraser River, Canada. *Sedimentary Geology* **85** (1-4), 25–37.

Le, H., Moin, P. & Kim, J. 1997 Direct numerical simulation of turbulent flow over a backward-facing step. *J. Fluid Mech.* **330**, 349–374.

Leonard, A. 1974 Energy cascade in large-eddy simulations of turbulent fluid flows. *Adv. Geophys.* **18A**, 237–248.

Maddux, T. B., McLean, S. R. & Nelson, J. M. 2003*a* Turbulent flow over three-dimensional dunes: 2. Fluid and bed stresses. *J. Geophys. Res.* **108(F1)**.

Maddux, T. B., Nelson, J. M. & McLean, S. R. 2003*b* Turbulent flow over three-dimensional dunes: 1. Free surface and flow response. *J. Geophys. Res.* **108(F1)**.

Matthes, G. H. 1947 Macroturbulence in natural stream flow. *Trans. American Ceophys. Union* **28** (2), 255–265.

McLean, S. R., Nelson, J. M. & Wolfe, S. R. 1994 Turbulence structure over two-dimensional bedforms: Implications for sediment transport. *J. Geophys. Res.* **99**, 12729–12747.

McLean, S. R. & Smith, J. D. 1986 A model for flow over two-dimensional bed forms. *J. Hydr. Engng* **112** (4), 300–317.

McLean, S. R., Wolfe, S. R. & Nelson, J. M. 1999 Predicting boundary shear stress and sediment transport over bed forms. *J. Hydr. Engng* **125** (7), 725–736.

Meneveau, C., Lund, T. S. & Cabot, W. H. 1996 A Lagrangian dynamic subgrid-scale model of turbulence. *J. Fluid Mech.* **319**, 353–385.

Müller, A. & Gyr, A. 1986 On the vortex formation in the mixing layer behind dunes. *J. Hydr. Res.* **24**, 359–375.

Nelson, J.M., McLean, S.R. & Wolfe, S.R. 1993 Mean flow and turbulence fields over two-dimensional bed forms. *Water Resour. Res.* **29** (12), 3935–3953.

Nelson, J. M. & Smith, J. D. 1989 Mechanics of flow over ripples and dunes. *J. Geophys. Res.* **94** (C6), 8146–8162.

Nezu, I. & Nakagawa, H. 1993 *Turbulence in Open-Channel Flows*. Balkema.

Omidyeganeh, M. & Piomelli, U. 2011 Large-eddy simulation of two-dimensional dunes in a steady, unidirectional flow. *J. Turbul.* **12** (42), 1–31.

Parsons, D. R., Best, J. L., Orfeo, O., Hardy, R. J., Kostaschuk, R. & Lane, S. N. 2005 Morphology and flow fields of three-dimensional dunes, rio paraná, argentina: Results from simultaneous multibeam echo sounding and acoustic doppler current profiling. *J. Geophys. Res.* **110** (F04S03).

Polatel, C., Muste, M., Patel, V. C. & Stoesser, T. 2006 Free-surface response to large-scale bed roughness. In *The* 7^{th} *Int. Conf. on Hydroscience and Engineering*, pp. 1–11. Drexel University, College of Engineering.

Radhakrishnan, S., Piomelli, U. & Keating, A. 2008 Wall-modeled large-eddy simulations of flows with curvature and mild separation. *ASME J. Fluids Eng.* **130** (101203).

Radhakrishnan, S., Piomelli, U., Keating, A. & Silva Lopes, A. 2006 Reynolds-averaged and large-eddy simulations of turbulent non-equilibrium flows. *J. Turbul.* **7** (63), 1–30.

Rhie, C. M. & Chow, W. L. 1983 Numerical study of the turbulent flow past an airfoil with trailing edge separation. *AIAA J.* **21**, 1525–1532.

van Rijn, L. C. 1984 Sediment transport, part III: Bed forms and alluvial roughness. *J. Hydr. Engng* **110** (12), 1733–1754.

Robert, A. & Uhlman, W. 2001 An experimental study on the ripple dune transition. *Earth Surf. Processes Landforms* **26**, 615–629.

Roden, J. E. 1998 The sedimentology and dynamics of mega-dunes, Jamuna River, Bangladesh. PhD thesis, Univ. Leeds, Leeds, U.K.

Schindler, R. J. & Robert, A. 2005 Flow and turbulence structure across the ripple–dune transition: an experiment under mobile bed conditions. *Sedimentology* **52**, 627–649.

Schmeeckle, M. W., Shimizu, Y., Baba, H. & Ikezaki, S. 1999 Numerical and experimental investigation of turbulence over dunes in open-channel flow. *Monthly Rep. Civ. Eng. Res. Inst.* **551**, 2–15.

Silva Lopes, A. & Palma, J. M. L. M. 2002 Simulations of isotropic turbulence using a non-orthogonal grid system. *J. Comput. Phys.* **175** (2), 713–738.

Silva Lopes, A., Piomelli, U. & Palma, J. M. L. M. 2006 Large-eddy simulation of the flow in an S-duct. *J. Turbul.* **7** (11), 1–24.

Sirovich, L. & Karlsson, S. 1997 Turbulent drag reduction by passive mechanisms. *Nature* **388**, 753–755.

Spalart, P. R. & Watmuff, J. H. 1993 Experimental and numerical study of a turbulent boundary layer with pressure gradients. *J. Fluid Mech.* **249**, 337–371.

Stoesser, T., Braun, C., García-Villalba, M. & Rodi, W. 2008 Turbulence structures in flow over two-dimensional dunes. *J. Hydr. Engng* **134** (1), 42–55.

Venditti, J. G. 2007 Turbulent flow and drag over fixed two- and three-dimensional dunes. *J. Geophys. Res.* **112** (F04008).

Venditti, J. G. & Bauer, B. O. 2005 Turbulent flow over a dune: Green River, Colorado. *Earth Surf. Proc. Landf* **30**, 289–304.

Venditti, J. G. & Bennett, S. J. 2000 Spectral analysis of turbulent flow and suspended sediment transport over dunes. *J. Geophys. Res.* **105**, 22035–22047.

Venditti, J. G., Church, M. & Bennet, S. J. 2005 On the transition between 2D and 3D dunes. *Sedimentology* **52**, 1343–1359.

Yalin, M. S. 1964 Geometrical properties of sand waves. *J. Hydr. Div. Am. Soc. Civ. Engng* **90** (HY5), 105–119.

Yoon, J. Y. & Patel, V. C. 1996 Numerical model of turbulent flow over sand dune. *J. Hydr. Engng* **122(1)**, 10–18.

Yue, W., Lin, C.L. & Patel, V.C. 2005 Large eddy simulation of turbulent open-channel flow with free surface simulated by level set method. *Phys. Fluids* **17**, 025108.

Yue, W., Lin, C.-L. & Patel, V. C. 2006 Large-eddy simulation of turbulent flow over a fixed two-dimensional dune. *J. Hydr. Engng* **132** (7), 643–651.

Zedler, E. A. & Street, R. L. 2001 Large-eddy simulation of sediment transport: Current over ripples. *J. Hydr. Res.* **127**, 444–452.